A physically based description of floodplain inundation dynamics in a global river routing model

Dai Yamazaki,[1] Shinjiro Kanae,[2] Hyungjun Kim,[3,4] and Taikan Oki[1]

[1] Current global river routing models do not represent floodplain inundation dynamics realistically because the storage and movement of surface waters are regulated by small-scale topography rather than the commonly used spatial resolution of global models. In this study, we propose a new global river routing model, CaMa-Flood, which explicitly parameterizes the subgrid-scale topography of a floodplain, thus describing floodplain inundation dynamics. The relationship between water storage, water level, and flooded area in the model is decided on the basis of the subgrid-scale topographic parameters based on 1 km resolution digital elevation model. Horizontal water transport is calculated with a diffusive wave equation, which realizes the backwater effect in flat river basins. A set of global-scale river flow simulations demonstrated an improved predictability of daily-scale river discharge in many major world rivers by incorporating the floodplain inundation dynamics. Detailed analysis of the simulated results for the Amazon River suggested that introduction of the diffusive wave equation is essential for simulating water surface elevation realistically. The simulated spatiotemporal variation of the flooded area in the Amazon basin showed a good correlation with satellite observations, especially when the backwater effect was considered. The improved predictability for daily river discharge, water surface elevation, and inundated areas by the proposed model will promote climate system studies and water resource assessments.

Citation: Yamazaki, D., S. Kanae, H. Kim, and T. Oki (2011), A physically based description of floodplain inundation dynamics in a global river routing model, *Water Resour. Res.*, *47*, W04501, doi:10.1029/2010WR009726.

1. Introduction

[2] The surface water cycle is an important component of the climate system. About 60% of total precipitation on land returns to the atmosphere via evapotranspiration, as a global average, whereas almost all the rest flows into the oceans or inland seas via river networks [*Oki and Kanae*, 2006]. Freshwater discharge from land to ocean plays a role in controlling the climate system by altering salinity in seawater and by affecting the thermohaline circulation [e.g., *Driscoll and Haug*, 1998]. Open water surfaces of lakes and wetlands also affect regional climate by altering the energy and water fluxes exchanged between land and atmosphere [e.g., *Coe and Bonan*, 1997; *Krinner*, 2003]. Given that wetlands have been identified as a major source of methane gas [*Houweling et al.*, 1999], gas emission from wetlands may have a significant impact on climate change in the long term. In addition to the impact of surface water on the climate system, understanding the spatial and temporal variation of the surface water cycle helps in water resource assessment because river discharge can be evaluated as a freshwater resource for human beings and other ecosystems [*Oki and Kanae*, 2006].

[3] Recent advances in satellite observation provide important information on various aspects of the storage and movement of surface water on the global scale, such as the extent of inundated areas [*Prigent et al.*, 2007; *Papa et al.*, 2010], water surface elevation [*Alsdorf et al.*, 2000, 2007], water depth and river discharge [*Andreadis et al.*, 2007; *Durand et al.*, 2008], and variations in terrestrial water storage [*Tapley et al.*, 2004]. However, such variations in the storage and movement of surface water are not adequately represented in global- or continental-scale river routing models, which are the only practical tool for simulating surface water transport in the major rivers of the world [e.g., *Miller et al.*, 1994; *Oki et al.*, 1999]. Global- or continental-scale river routing models have used relatively coarse resolution grids (about 10 km for continental scale, 50 or 100 km for global scale) mainly because of computational limitations. Because detailed topography, such as river channels, is not resolved in coarse-resolution grids, global- or continental-scale river routing models have not represented the physical process of horizontal water transport, i.e., flow computation based on the gradient of terrain surface that can be resolved in the models. Instead, they calculate horizontal water transport along a prescribed river

---

[1]Institute of Industrial Science, University of Tokyo, Tokyo, Japan.
[2]Department of Mechanical and Environmental Informatics, Tokyo Institute of Technology, Tokyo, Japan.
[3]UC Center for Hydrologic Modeling, University of California, Irvine, California, USA.
[4]Also at Institute of Industrial Science, University of Tokyo, Tokyo, Japan.
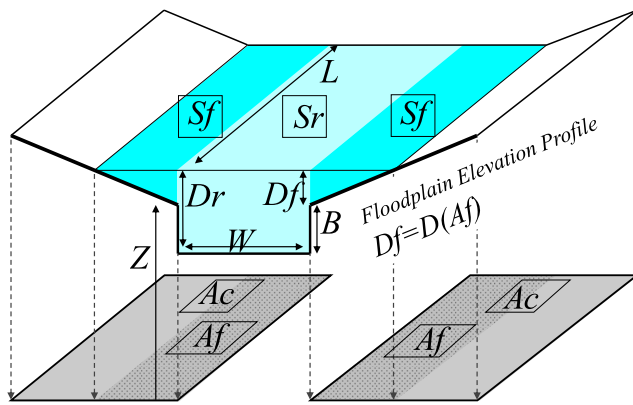
Figure 1. Illustration of a river channel reservoir and a floodplain reservoir defined in each grid. Parameters and variables are listed in Table 1.

network map which is manually delineated on the basis of available digital elevation models (DEMs) and world atlases [e.g., *Oki and Sud*, 1998; *Döll and Lehner*, 2002]. Furthermore, the explicit representation of inundated area and water depth, which is also controlled by much smaller scale topography than the resolution of continental- and global-scale models, is almost impossible.

[4] Fine-resolution (≤1 km) global DEMs, which might be detailed enough to explain surface water dynamics in continental-scale rivers [*Sanders*, 2007], are already acquired on the basis of satellite remote sensing. For example, Shuttle Rader Topography Mission (SRTM) (http://www2.jpl.nasa.gov/srtm/) and Advanced Spaceborne Thermal Emission and Reflection Radiometer global digital elevation model (ASTER DEM) (http://www.ersdac.or.jp/GDEM/E/index.html) provide considerably fine resolution (90 and 30 m, respectively) global DEMs. In addition, fine-resolution flow direction maps are derived from these DEMs, such as HydroSHEDS and HYDRO1k, which have resolutions of 90 and 1 km, respectively [*Lehner et al.*, 2008]. By using these or much higher resolution DEMs, river routing models for small basins resolve terrain surface for explicitly simulating inundation dynamics [e.g., *Dutta et al.*, 2000; *Bates and De Roo*, 2000; *Wilson et al.*, 2007; *Biancamaria et al.*, 2009]. While small-basin models can be scaled up, the computational cost of doing this globally is likely to be prohibitive if the routing algorithm needs to be part of a larger Earth system or global climate model.

[5] Instead, some global- or continental-scale models treat surface water dynamics as subgrid-scale phenomena. One strategy is the conceptual representation of surface water reservoirs such as floodplains, lakes, and wetlands [e.g., *Coe et al.*, 2002; *Döll et al.*, 2003]. This approach significantly improves the models' ability to reproduce seasonal variations in river discharge. However, the precise representation of surface water stages, such as water depth and inundated area, has not been achieved because the detailed topography of river channels and floodplains is required to estimate water stage variation in the subgrid scale. Advanced models calculate the relationship between water volume and flooded area using subgrid topography [*Coe et al.*, 2008; *Decharme et al.*, 2008] for the explicit prediction of inundated area. However, water surface ele-

vation and slope were estimated on the basis of statistical parameters such as average or standard deviation within a grid box, which do not always reflect the relationship between river stage and surface waters movements. In this paper, we have improved these approaches and propose an advanced method for describing the relation between water volume, flooded area, and river stage using subgrid-scale topography.

[6] A detailed description of the model framework and the method for describing subgrid-scale topography in river channel and floodplain are provided in section 2. This newly developed model, the Catchment-Based Macro-scale Floodplain (CaMa-Flood) model was tested by comparing the results of surface water simulation against in situ and satellite observations.

2. Model Framework

[7] CaMa-Flood is a distributed global river routing model that routes input runoff generated by a land surface model to oceans or inland seas along a prescribed river network map. It calculates river and floodplain water storage, river discharge, water depth, and inundated area for each grid point. Water storage is the only prognostic variable, and the other variables are diagnosed from water storage. The resolution of the model was fixed to 15 arc min (about 25 km) in this paper, but it can be easily modified.

[8] Each grid point has a river channel reservoir and a floodplain reservoir, as illustrated in Figure 1. Note that the floodplain reservoir consists of the unit catchment of the river channel for each grid point (i.e., the area from which the river collects runoff; see area divided by the thick black boundary in Figure 2b), so that some areas that might never be flooded are also included in the floodplain reservoir. River channel and floodplain are treated as continuous reservoirs in that water spilling from the river channel is stored in the floodplain. This idea of assuming polygonal storages for river channels and floodplains has been adapted to some hydrological or hydrodynamics models in order to represent the realistic relationship between water storage and stage [e.g., *Zanobetti et al.*, 1970; *Bates*, 2000].

[9] The parameters and variables used in CaMa-Flood are listed in Table 1. A river channel reservoir has three parameters: channel length, L, channel width, W, and bank height, B. A floodplain reservoir has a parameter for unit catchment area, A_c, and a floodplain elevation profile, $D_f = D(A_f)$, which describes floodplain water depth, D_f, as a function of flooded area, A_f. For simplification, D_f is given as an increasing function of A_f (see Figure 2c) so that no local depression is assumed in the floodplain elevation profile. This simplification was based on the assumption that inundation always occurs from lower to higher places within a unit catchment. Note that all topographic depressions, including permanent lakes and wetlands, are treated as "floodplain storages" within the framework of CaMa-Flood. In section 3, we explain how we defined those topographic parameters.

[10] River channel water storage, S_r, floodplain water storage, S_f, river channel water depth, D_r, floodplain water depth, D_f, and flooded area, A_f, are diagnosed from the total water storage of a grid point, S, by solving simultaneous equations (1) or (2) below. One of the simulta-
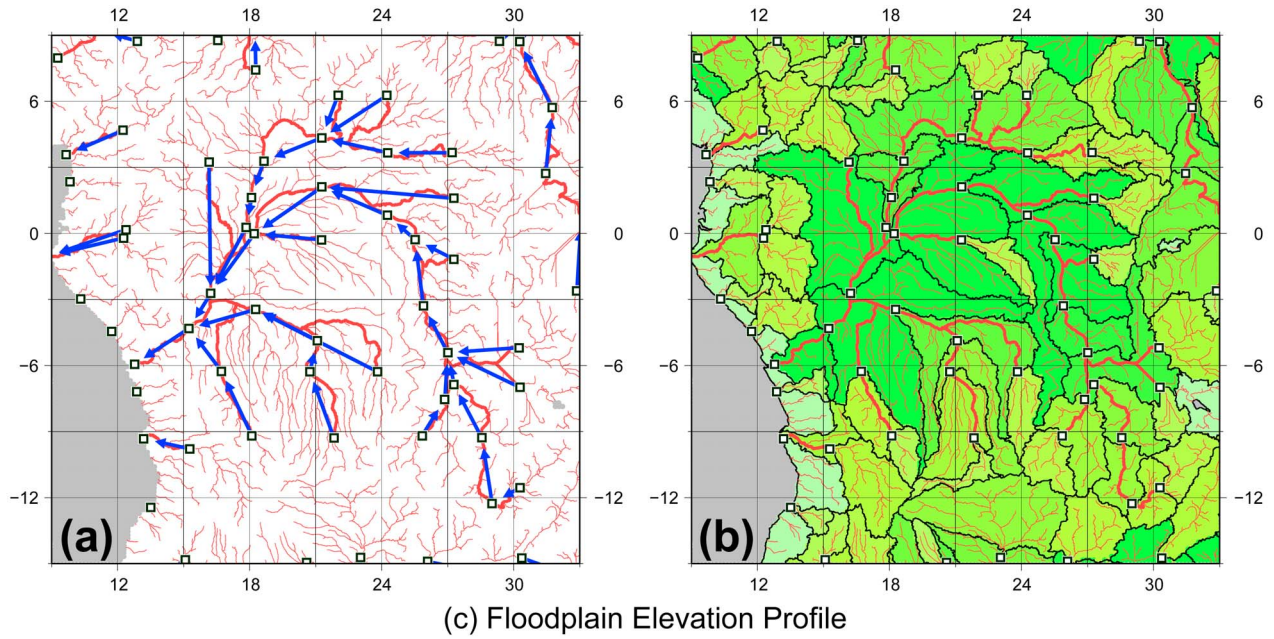
(c) Floodplain Elevation Profile

Figure 2. River networks and subgrid topographic parameters derived from fine-resolution DEM and flow direction maps. (a and b) Small squares indicate outlet pixels, and thick lines indicate river channel pixels. Vectors in Figure 2a indicate the downstream direction of each grid. Areas divided by black boundaries in Figure 2b indicate the unit catchment. (c) The thick gray line indicates the cumulative distribution function (CDF) of the SRTM30 elevation within a unit catchment, and the thin line connecting each 10th percentile of the CDF represents the simplified function for the floodplain elevation profile.

neous equations (1) or (2) is chosen by comparing the total water storage, S, against the flood initiation storage, $S_{ini} = BWL$, where B is bank height, W is channel width, and L is channel length. For cases in which total water storage, S, is less or equal to the flood initiation storage, S_{ini},

$$\begin{aligned} S_r &= S \\ D_r &= \frac{S_r}{WL} \\ S_f &= 0 \\ D_f &= 0 \\ A_f &= 0. \end{aligned} \quad (1)$$

For cases in which total water storage, S, is greater than the flood initiation storage,

$$\begin{aligned} S_r &= S - S_f \\ D_r &= \frac{S_r}{WL} \\ S_f &= \int_0^{A_f} \left(D_f - D(A)\right) dA \\ D_f &= D_r - B \\ A_f &= D^{-1}\left(D_f\right). \end{aligned} \quad (2)$$

The equation $D_f = D_r - B$ in (2) means that the water surface elevations of the river channel and the floodplain are the

Table 1. List of Parameters and Variables

Symbol	Name	Unit
Parameters		
L	channel length	m
W	channel width	m
B	bank height	m
Z	surface altitude	m
X	distance to downstream cell	m
A_c	unit catchment area	m^2
n	Manning's roughness coefficient	m$^{-1/3}$/s
Variables		
S	total water storage, Sr + Sf	m^3
S_r	river channel water storage	m^3
S_f	floodplain water storage	m^3
D_r	river water depth	m
D_f	floodplain water depth	m
H	effective river depth	m
A_f	flooded area	m^2
R	runoff from land surface model	m/s
Q	discharge	m^3/s
R_{up}	maximum 30 day upstream runoff	m^3/s
v	river flow velocity	m/s
i_0	riverbed slope	-
i_{sfc}	water surface slope	-
i_f	friction slope	-

same. This equation is based on the assumption that water mass is instantaneously exchanged between the channel and the floodplain to balance the water surface elevations of the two reservoirs. The function $D^{-1}(D_f)$, which is the inverse function of $D(A_f)$, describes flooded area, A_f, as a function of floodplain water depth, D_f (see Figure 2c). The simultaneous equations (2) are solvable because the elevation profile function, $D_f = D(A_f)$, was assumed to be an increasing function.

[11] In addition, channel altitude, Z (i.e., the elevation of the top of the bank; see Figure 1), and distance to the downstream grid point, X, are parameterized for each grid point. These two topographic parameters are used for calculating the water surface slope toward a downstream grid point.

[12] Horizontal water transport between grid points is calculated along a prescribed river network map, which indicates a downstream grid point for each grid point. Each grid point was assumed to have only one downstream grid point, so that river discharge is solved along one-dimensional streamlines. The river division was not expressed by this assumption. However, division is only dominant in delta areas near river mouths, so the impact of neglecting this is not significant in global-scale modeling. Horizontal water transport between grid points is only calculated for river channels because water exchange between floodplains is considered to be much smaller than river discharge (i.e., water flux in river channels) [*Alsdorf et al.*, 2010].

[13] River discharge for each grid point is calculated by a diffusive wave:

$$\partial D_r / \partial x + i_0 - i_f = 0, \quad (3)$$

where D_r is river water depth, x is distance along river channel, i_0 is riverbed slope, and i_f is friction slope. The diffusive wave equation is a simplification of the full one-dimensional St. Venant momentum equation, in which

acceleration and advection terms are neglected. Those terms are very small compared to the pressure, bed slope, and friction slope terms of equation (3) in the case of the streamflow in large rivers represented in CaMa-Flood [see *Moussa and Bocquillon*, 1996]. Hence, the diffusive wave approximation is considered to be acceptable for the governing equation for momentum conservation in a global river routing model. Summation of the first and second terms yields water surface slope, i_{sfc}, which is described as

$$i_{sfc} = \frac{(Z_i - B_i + D_{r_i}) - (Z_j - B_j + D_{r_j})}{X_i}. \quad (4)$$

Indices i and j refer to the target grid point and its downstream grid point, respectively. X_i is the distance to the downstream grid point. The term $Z_i - B_i + D_{r_i}$ represents the water surface elevation of grid i (see Figure 1). Because the diffusive wave equation estimates flow velocity on the basis of water surface slope, the backwater effect is represented (i.e., the water stage downstream affects flow velocity upstream).

[14] Friction slope, i_f, is given by

$$i_f = n^2 v^2 H^{-\frac{4}{3}}, \quad (5)$$

where n is Manning's roughness coefficient, v is flow velocity, and H is hydraulic radius. Manning's roughness coefficient is fixed to 0.03 for all rivers. The sensitivity of the model to the Manning's coefficient is discussed in section 6. Given that river width is much larger than river depth in continental-scale rivers, hydraulic radius was approximated by effective water depth, or the depth of the cross section where water can pass through between the target grid point, i, and its downstream grid point, j. Effective water depth, H, is given by

$$H = \max\left[D_{r_i}, (Z_j - B_j + D_{r_j}) - (Z_i - B_i)\right]. \quad (6)$$

The second term, $(Z_j - B_j + D_{r_j}) - (Z_i - B_i)$, within the maximum function of equation (6) is required when water surface elevation is higher in downstream than upstream and when backward flow occurs [*Horritt and Bates*, 2002]. By substituting equation (5) into equation (3), flow velocity, v, is derived as

$$v = \frac{i_{sfc}}{|i_{sfc}|} n^{-1} i_{sfc}^{\frac{1}{2}} H^{\frac{2}{3}}. \quad (7)$$

Note that positive velocity indicates forward flow from upstream to downstream, whereas negative velocity indicates backward flow from downstream to upstream. Finally, river discharge, Q, is derived as the product of flow velocity and cross-sectional area, $A = HW$:

$$Q = Av = HWv. \quad (8)$$

Note that the cross-sectional area, $A = HW$, represents the cross section of a river channel, so that flow velocity is effective only on the river channel storage but not on the floodplain storage (see Figure 1).

[15] The time evolution of water storage for each grid point, S_i, is predicted by the continuative equation (9) considering river discharge to the downstream grid point, river

discharge from the upstream grid point(s), and input runoff from the land surface model, R_i:

$$S_i^{t+\Delta t} = S_i^t + \sum_k^{\text{upstream}} Q_k^t \Delta t - Q_i^t \Delta t + A_{c_i} R_i^t \Delta t, \qquad (9)$$

where t is time and Δt is time step. The index k indicates each upstream grid point of the target grid point i. The detailed computation methods for preserving water balance and reducing numerical instability are summarized in Appendix A.

3. A River Network Map and Topographic Parameters

[16] The subgrid topographic parameters of CaMa-Flood (Figure 1) define the relationship between total water storage within each grid point and water stage, such as water depth and inundated area. Therefore, realistic delineation of the parameters is paramount for the precise modeling of surface water dynamics. In this paper, the Flexible Location of Waterways (FLOW) method [Yamazaki et al., 2009] was applied to delineate topographic parameters and a river network map for CaMa-Flood from a fine-resolution (1 km) flow direction map and DEM.

[17] As an input fine-resolution flow direction map, the Global Drainage Basin Database (GDBD) [Masutomi et al., 2009] was used in this study. GDBD describes the downstream direction of each pixel at 1 km resolution in raster format and covers the global range except Greenland and Antarctica. Each GDBD pixel is assumed to have only one downstream direction toward one of the eight neighboring pixels.

[18] The SRTM30 DEM (the 30 arc sec DEM developed in the Shuttle Rader Topography Mission by NASA) was employed as an input DEM for the FLOW method. The SRTM30 is one of the most accurate DEMs covering almost the entire globe and has a comparable spatial resolution to GDBD. Because of the difference in geometric projection between GDBD and SRTM30, SRTM30 DEM was spatially interpolated to create a surface elevation map with the same grid coordinate as GDBD. To remove the inland sinks, which interfered with flow going downstream in the surface elevation map, the elevation profile along river channels of GDBD was smoothed by the algorithm explained in Appendix B. The SRTM30 DEM also has a systematic error due to surface artifacts such as vegetation [Sun et al., 2003], but it is practically impossible to clean up those errors globally. Hence, the SRTM DEM was used without any correction on the vegetation errors in this study.

[19] The procedures for delineating coarse-resolution river network parameters for CaMa-Flood from the fine-resolution DEM and flow direction map by the FLOW method are explained in Figure 2. Fine-resolution river paths in Figures 2a and 2b were derived from 1 km resolution GDBD. As an example, the resolution of the river network map for CaMa-Flood was set to 3° (about 300 km) in Figure 2, but the FLOW method can be applied to delineate a river network map at any resolution. For the simulations in this paper, a 15 arc min (about 25 km) river network map was generated. In this section, fine-resolution grid elements are termed "pixels," and coarse-resolution grid elements are termed "cells" for clarity. For the explanation of parameter delineation with detailed figures, see the description paper of the FLOW method [Yamazaki et al., 2009].

[20] First, a river network map for CaMa-Flood was created from GDBD. One GDBD pixel within each cell was marked as the outlet pixel of the cell (a pixel marked with a small square in Figure 2a). The outlet pixel was decided by the criteria of the FLOW method, which basically chose the pixel with the maximum upper drainage area within the cell. The fine-resolution river channel of GDBD was traced from the outlet pixel of a target cell until it reached the next outlet pixel downstream. The coarse-resolution cell where the next outlet pixel was located was determined to be the downstream cell of the target cell (the downstream cell of each cell is indicated with a vector in Figure 2a). Note that the downstream cell was not necessarily selected from the eight cells neighboring the target cell but was located on any cell. The exception was if the traced river channel reached a coastal pixel of GDBD, then the target cell was recognized as a river mouth cell.

[21] Second, channel altitude (i.e., the elevation of the upper edge of river bank), Z, was defined as the elevation of the outlet pixel for each cell. Because channel altitude for each cell was derived from the pixel on a river channel of GDBD, it never caused "negative slope," which would impede river flow. Thus, CaMa-Flood has smaller uncertainties with surface altitude compared to previous river routing models that employ averaged elevation within a cell as channel altitude.

[22] Then, the channel length, L, of each cell was determined as the length of the fine-resolution river channel between the outlet pixels of the cell and its upstream cell (thick lines denoting river channels within each unit catchment in Figure 2b). Where multiple upstream cells exist for one cell, the upstream outlet pixel with largest drainage area was chosen as the representative upstream outlet pixel. For headwater cells with no upstream cell, channel length was given as a half length of the cell size. Channel length, derived by the FLOW method, considered the meandering of a river channel at the scale of the 1 km resolution flow direction map. This method realizes objective representation of river meandering in subgrid scale. Similarly, distance to a downstream grid point, X, was decided as the length of the fine-resolution river channel meandering between the outlet pixels of the cell and its downstream cells.

[23] Next, the group of GDBD pixels that drained into the outlet pixel of each cell was determined as the unit catchment pixels of the cell (pixels divided by black boundaries in Figure 2b). The total area of the unit catchment pixels for each cell was determined as the catchment area, A_c, for the cell. In CaMa-Flood, river flow simulation is done on the basis of this unit catchment element instead of the traditional rectangular grid box.

[24] The cumulative distribution function (CDF) of the elevation within each unit catchment was taken to describe the floodplain elevation profile (see the thick gray line in Figure 2c). The horizontal axis of Figure 2c is the flooded area fraction (i.e., percentage of flooded area, A_f, within the unit catchment, A_c). This CDF describes the relationship between a flooded area, A_f, and floodplain water depth, D_f, under the assumption that inundation occurs from lower to higher areas within the unit catchment. To reduce computational load, every tenth percentile of CDF (dots in Figure 2c) was extracted, and the line connecting these points (thin line
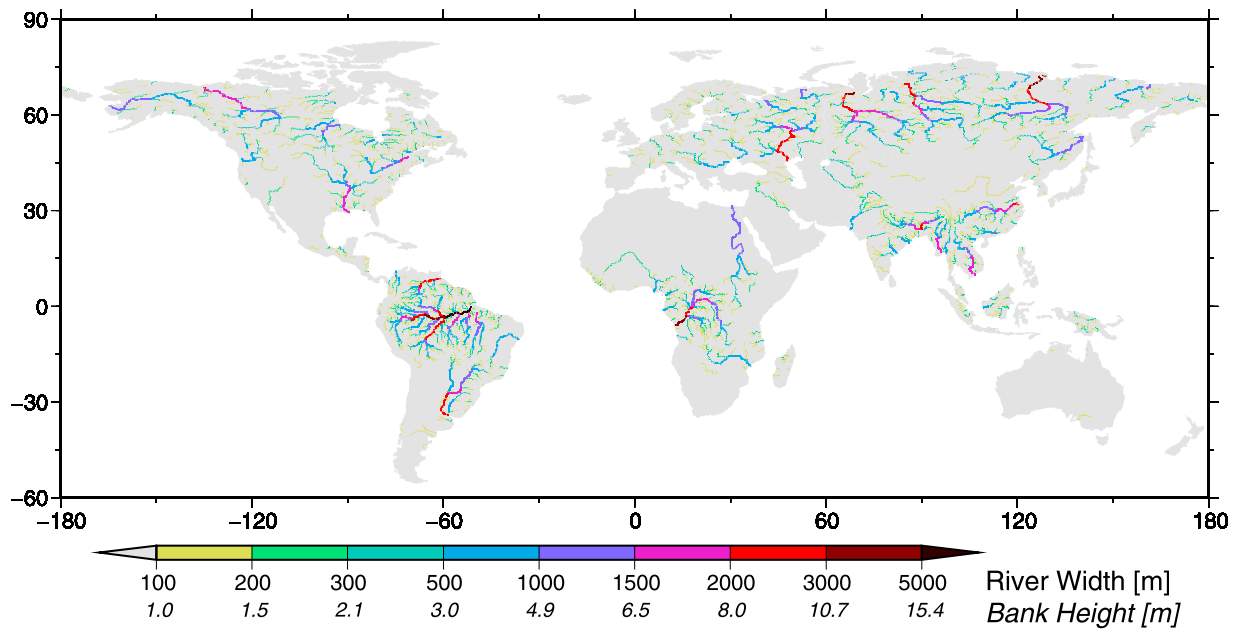
Figure 3. River channel width and bank height estimated from monthly based upstream runoff.

in Figure 2c) was determined as a function to describe the floodplain elevation profile, $D_f = D(A_f)$.

[25] Channel width, W, and bank height, B, are not resolved in GDBD and SRTM30. Hence, they were empirically determined as a function of maximum 30 day upstream runoff, R_{up} (m^3/s). R_{up} was calculated from the river network map and the climatology of daily runoff estimated by a land surface model [*Kim et al.*, 2009]. The identical empirical functions were used for all the rivers represented in the river network map (i.e., parameters were not calibrated for each river) because observation data sets for calibration are not available for all the rivers.

[26] Channel width, W (m), and bank height, B (m), were estimated by

$$W = \max\left[1.00 \times R_{up}^{0.7}, 10.0\right] \qquad (10)$$

$$B = \max\left[0.035 \times R_{up}^{0.5}, 1.00\right]. \qquad (11)$$

The parameters in equations (10) and (11) were carefully calibrated by trial and error. River width and bank height estimated by equations (10) and (11) are shown in Figure 3. The sensitivity of the river routing model to channel width and bank height is discussed in section 6.

[27] Using these topographic parameters, river water storage, S_r, floodplain water storage, S_f, river water depth, D_r, floodplain water depth, D_f, flooded area, A_f, and water surface slope to downstream grid, i_{sfc}, are calculated from total water storage, S.

4. Experiment Design

[28] Three experiments with different model settings (FLD+Diff, FLD+Kine, and NoFLD) were run. FLD+Diff was the control for CaMa-Flood that considered both river channel and floodplain reservoirs and adopted the diffusive wave equation as the governing equation for flow computation. FLD+Kine used a kinematic wave equation instead of the diffusive wave equation to assess the impact of backwater effect, which is represented only by the diffusive wave equation. NoFLD did not include a floodplain reservoir and assumed an infinite bank height, B, to assess the impact of a floodplain reservoir on river flow. NoFLD adopted a kinematic wave equation as the governing equation.

[29] Flow velocity by the kinematic wave equation is given as

$$v = n^{-1} i_0^{\frac{1}{2}} H^{\frac{2}{3}}, \qquad (12)$$

where v is flow velocity, n is Manning's coefficient, i_0 is riverbed slope, and H is effective water depth (or hydraulic radius). Because flow velocity is estimated on the basis of riverbed slope, the backwater effect is not represented.

[30] The spatial resolution of the river network map was set to 15 arc min, and the time steps were set to 20 min for FLD+Diff and 30 min for FLD+Kine and NoFLD. The time step for FLD+Diff was carefully selected to avoid numerical instability. Input runoff was determined using a land surface model and climate forcing data sets such as observed or reanalysis-based precipitation, temperature, surface pressure, and so on [*Kim et al.*, 2009]. Input runoff was prepared for each 1° grid box. Each unit catchment of CaMa-Flood received input runoff from the 1° grid box where the outlet pixel of the unit catchment was located. The unit of input runoff (m/s) was converted to water volume (m^3/s) by multiplying by the unit catchment area (m^2) as described in equation (9). This procedure does not precisely mirror the total amount of input runoff calculated on the basis of rectangular grid boxes because of the discrepancy in the grid element boundaries between rectangular grid boxes and unit catchments. However, the main purpose of this study was to examine the difference in surface water dynamics simulated by each experiment, so the discrepancy
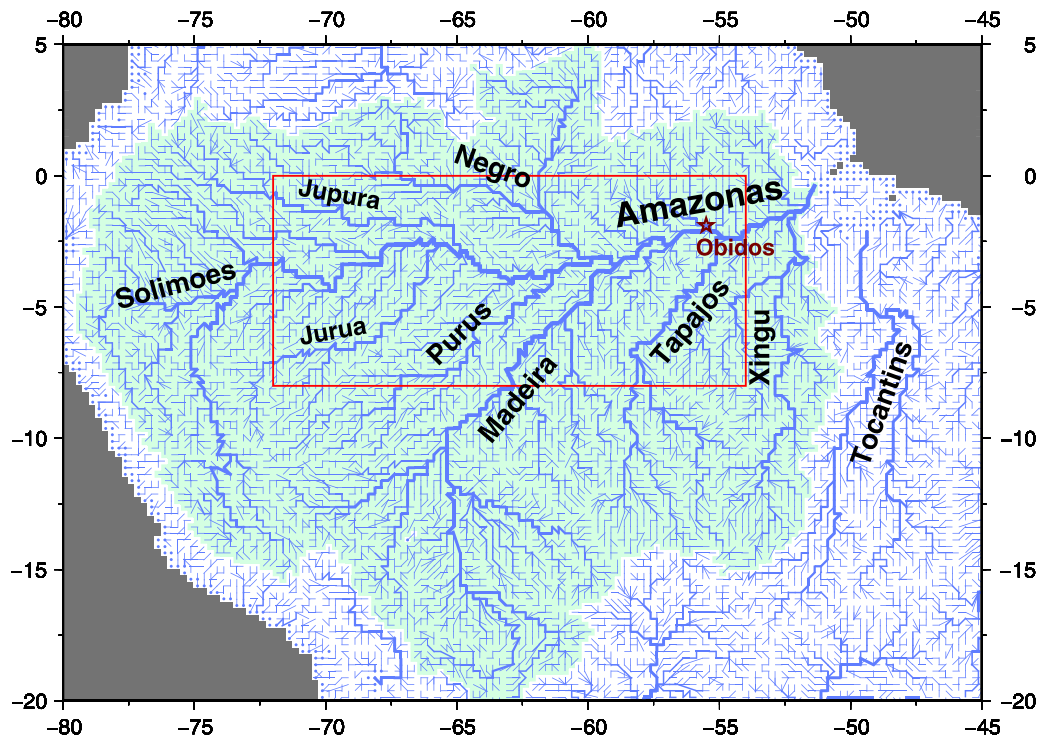
Figure 4. The river network map for the Amazon River. Obidos gauging station is marked with a star. The area in the rectangle is the domain for the validation of flooded area in Figures 8 and 9.

in the elements boundaries was not important. The simulation was over a 21 year period from 1980 to 2000; 1980 was used for spin-up, and the other 20 years were used for validation.

[31] A boundary condition at the river mouth was required for FLD+Diff because information from the downstream river stage was necessary for the diffusive wave equation. In this study, the distance from river mouth to ocean was fixed at 10 km, and the water surface elevation of ocean was the same as the elevation of the top of the bank at the river mouth grid point. However, the kinematic wave equation does not require a downstream boundary condition because this information is not necessary for flow computation.

5. Results

[32] Simulated results for the Amazon River were extensively analyzed to assess the detailed characteristics of the developed model. Then the results for major world river basins were shown to verify the model's ability with respect to global-scale simulation.

5.1. The Amazon River

[33] The simulated results for the Amazon River basin were validated against in situ and satellite observations. The Amazon River has the largest floodplain in the world along its main stem; therefore, significant improvements of simulated hydrological cycles were expected by introducing a floodplain reservoir. The river network map for the Amazon River is shown in Figure 4.

[34] Figure 5a illustrates observed and simulated daily river discharge from 1993 to 1995 at Obidos, the gauging station about 800 km upstream from the river mouth. The validation time span was decided according to the availability of daily river discharge observation. The thick gray line indicates observed river discharge according to data from the Global Runoff Data Center (GRDC). The lines marked with circles, squares, and triangles indicate simulated discharge by FLD+Diff, FLD+Kine, and NoFLD, respectively. The averaged discharge is 177,800 m/s by observation and 194,400 m/s by simulation; therefore, the total river discharge in the simulation was 9% larger than actual observed data.

[35] Simulated river discharge by NoFLD, which did not include a floodplain reservoir, showed larger perturbations than other experiments when compared with actual observed data. It is found from Figures 5b and 5c, which illustrate water depth and river flow velocity variations at the Obidos gauging station, that the change in water levels was overestimated during flood events in NoFLD because water is stored only in the rectangular river channel. Because flow velocity increases when water level is high according to the kinematic wave equation (12), water is immediately discharged downstream. Alternatively, the fluctuation in daily river discharge was suppressed in FLD+Kine and FLD+Diff (Figure 5a), which included a floodplain reservoir. The floodplain reservoir stores the water that spills out of the river channel; hence, the unrealistic perturbation of the water level was suppressed (Figure 5b). The range of simulated water level variation was about 7 m by FLD+Diff (Figure 5b), which is very close to the observed value of 6.94 m [*Alsdorf et al.*, 2010].

[36] Even though daily river discharges from FLD+Kine and FLD+Diff showed similar pattern at the Obidos, the flow regimes were different in the Amazon tributaries in those experiments. Figure 6 illustrates the river flow velocity
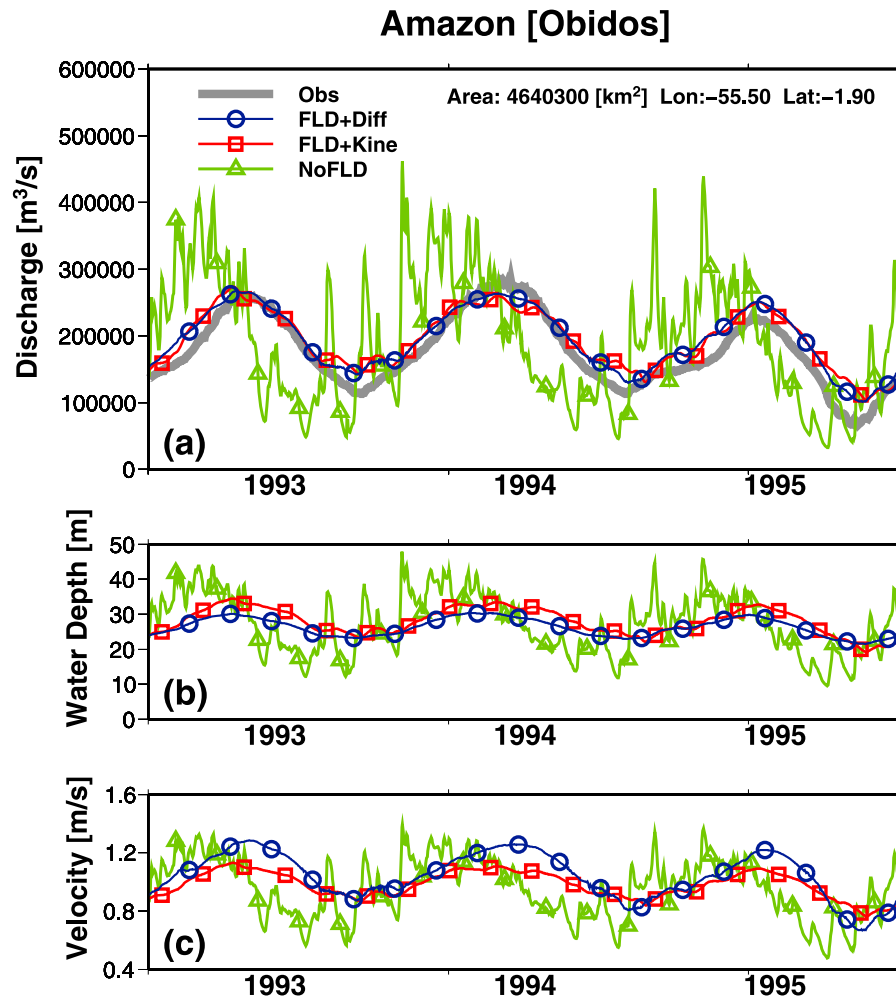
Amazon [Obidos]

Figure 5. (a) Observed and simulated daily river discharge, (b) simulated water depth, and (c) simulated river flow velocity at Obidos gauging station, the Amazon River. Thick gray line represents observation by GRDC. The lines marked with circles, squares, and triangles indicate simulation by FLD+Diff, FLD+Kine, and NoFLD, respectively.

averaged for May 1993, high-water season in the Amazon River. Water level in the mainstream is so high in May that inflow from branches is slowed because of the backwater effect [*Meade et al.*, 1991; *Trigg et al.*, 2009]. Flow velocity in branches was estimated to be slower in FLD+Diff compared with the simulated velocity by FLD+Kine (Figure 6). Even though the seasonal patterns of simulated daily river discharge were similar (correlation coefficients between observation and simulation were 0.97 and 0.95 for FLD+Diff and FLD+Kine, respectively), the detailed process of hydrological cycles in the Amazon River was represented better by FLD+Diff.

[37] The simulated flow velocity by FLD+Diff was about 1.0–1.5 m/s along the main stem (Figure 6a), which is larger than the estimated values by previous models (0.3–0.5 m/s) [e.g., *Miller et al.*, 1994; *Oki et al.*, 1999]. However, the models used in these studies assumed that flow velocity is constant for space and time, while the velocity in CaMa-Flood varies in space and time. Given that May is the high-water season in the Amazon, the flow velocity shown in Figure 6 must be faster than the annual average.

[38] Furthermore, the velocity defined in the previous studies was "effective velocity," which is applied to the total

water storage in a grid [e.g., *Miller et al.*, 1994; *Oki et al.*, 1999]. The flow velocity in CaMa-Flood is effective only on river storage but not on total water storage, which is the summation of the river storage and the floodplain storage as shown in Figure 1. Hence, the flow velocity in CaMa-Flood can be bigger than the effective velocity in previous models. For example, the velocity of FLD+Kine (Figure 6b) was generally faster than that of NoFLD (Figure 6c) because the flow velocity in NoFLD, which did not consider floodplain storages, was applied to the total water storage. The flow velocity in the experiments with floodplains is better for comparison with in situ observed velocity than effective velocity in previous models. Direct observations of river flow velocity are limited in the Amazon basin, but available data have shown that river flow velocity can be faster than 1.5 m/s in the mainstream and major tributaries [e.g., *Meade et al.*, 1991; *Filizola and Guyot*, 2004].

[39] There is another difference in the spatial pattern of flow velocity estimated by FLD+Diff and FLD+Kine. Flow velocity by FLD+Diff (Figure 6a) gradually varied along the mainstream because water surface elevation was adjusted between upstream and downstream by the dissuasive wave equation. When the difference in elevation between upstream
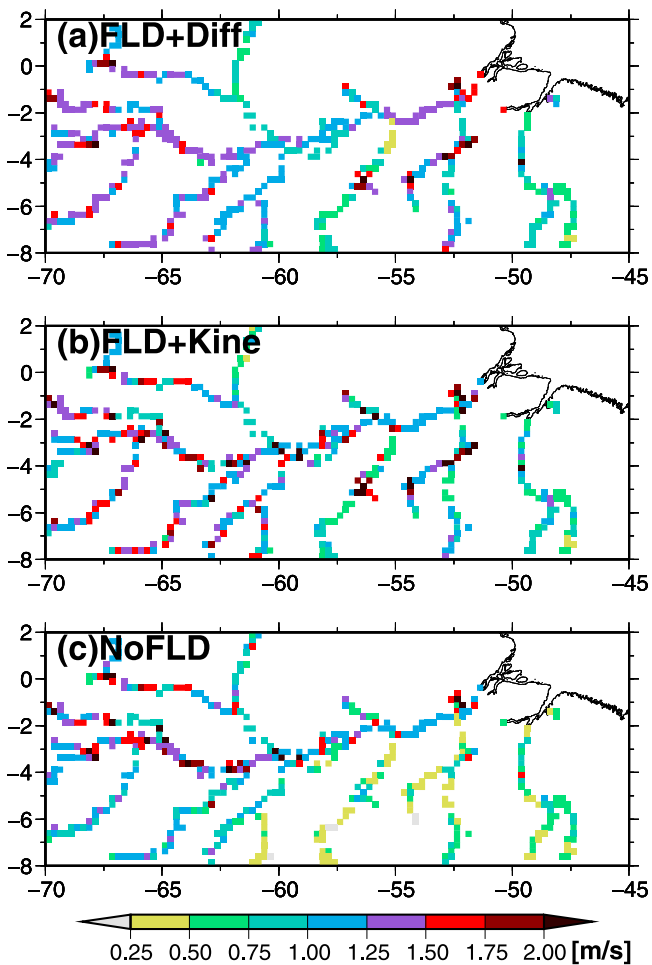
Figure 6. River flow velocity averaged for May 1993. Simulation results by (a) FLD+Diff, (b) FLD+Kine, and (c) NoFLD are shown. River channels whose upstream drainage area smaller than 5000 km^2 are masked.

and downstream is large, the water surface slope of the stream is steep and flow velocity is high. When the difference in elevation is small, the flow velocity is low and, consequently, the difference in water surface elevation between upstream and downstream decreases; thus, smooth flow velocity was predicted along the mainstream in FLD+Diff. On the other hand, flow velocity is determined by a local riverbed slope in the kinematic wave equation, so in FLD+Kine, a grid point with a steep local gradient always showed faster flow velocity than grid points with a mild local gradient (Figure 6b).

[40] Uneven flow velocity also generated uneven water surface elevation along river networks with FLD+Kine and NoFLD. In the worst cases, some grid points had a negative water surface slope (i.e., water surface altitude was lower upstream than downstream). The profiles of monthly averaged water surface elevation in May 1993 along the Amazon main stem are shown in Figure 7a. Black and gray lines indicate the elevations of the bottom and top of the river bank, respectively. The lines marked with circles, squares, and triangles indicate the water surface elevation simulated by FLD+Diff, FLD+Kine, and NoFLD, respectively. The water surface profile of FLD+Diff was smooth along the main stem, while those of FLD+Kine and NoFLD were uneven. In the kinematic wave equation, flow velocity is estimated to be faster at a grid with a steep slope than a grid with a mild slope. Since water is immediately discharged from the grid with a steep slope, the water surface elevation of FLD+Kine and NoFLD drops where the bed slope is large (see the bed slope profile in Figure 7b).

[41] Besides river discharge, a simulated flooded area was validated using satellite observations. Figure 8 illustrates a simulated and observed flooded area fraction, i.e., percentage of flooded area within each unit catchment. Figure 8 (top) represents the low-water season (September-October 1995), and Figure 8 (bottom) represents high-water season (May-June 1996). Figure 8a represents the observed flooded area using SAR-derived data sets [Hess et al., 2003], whereas
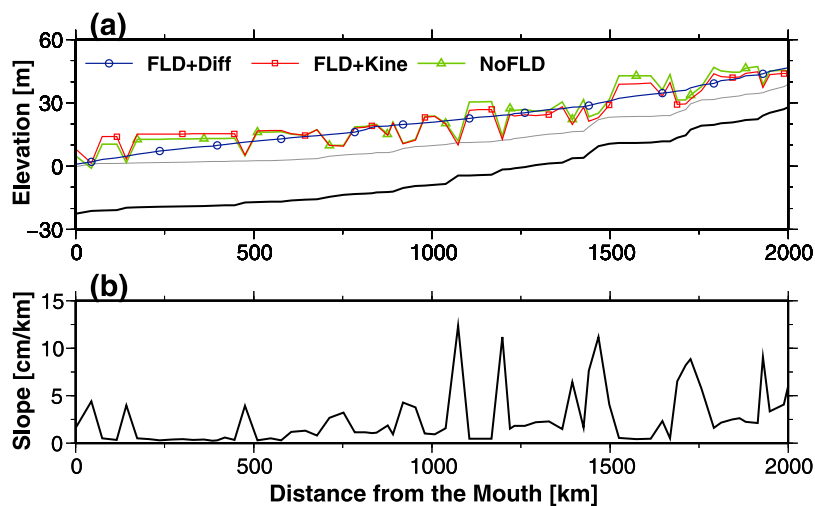

Figure 7. (a) Monthly averaged water surface elevation in May 1993 and (b) bed slope along the Amazon main stem. Black and gray lines in Figure 7a indicate elevations of riverbed and top of bank, respectively. The lines marked with circles, squares, and triangles indicate water surface elevation simulated by FLD+Diff, FLD+Kine, and NoFLD, respectively.
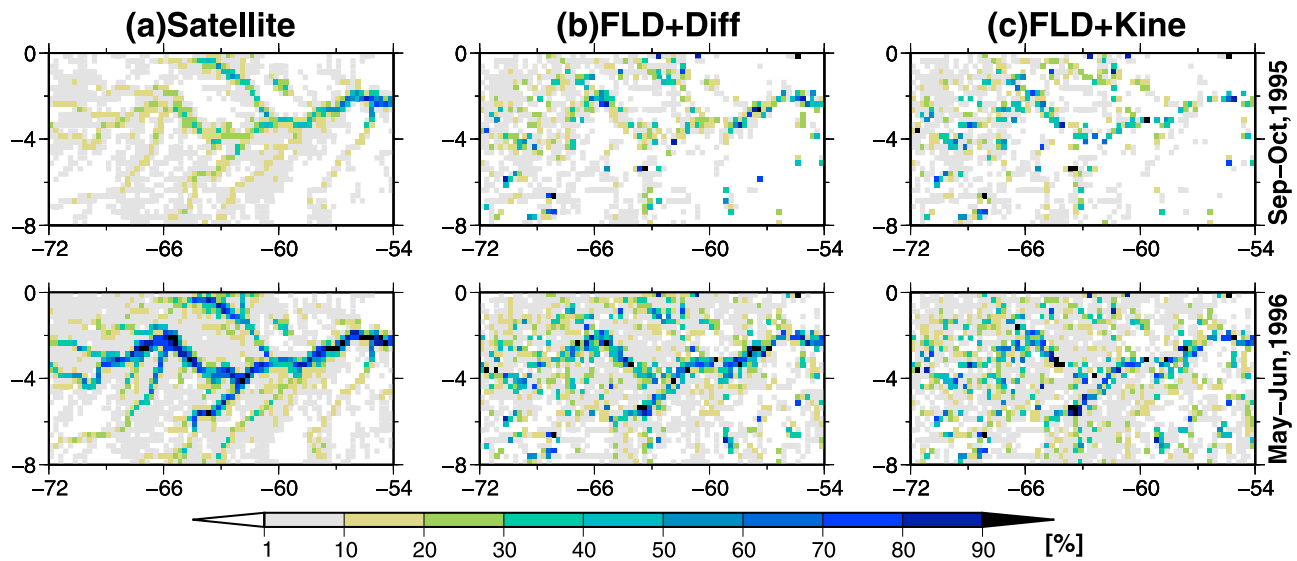
Figure 8. Flooded area fraction in the Amazon River basin for (top) September-October 1995 and (bottom) May-June 1996: (a) satellite observation [*Hess et al.*, 2003], (b) FLD+Diff, and (c) FLD+Kine.

Figures 8b and 8c represent a simulated flooded area by FLD+Diff and FLD+Kine, respectively. The SAR-derived flooded area by Hess et al. was originally provided at the 90 m resolution, and it was integrated into the 15 arc min resolution for comparison with the model simulation. The comparison of the illustrated flooded area fraction between simulation and observation is not rigorous because of the non-rectangular unit catchment as defined in CaMa-Flood, but the general pattern of floodplain inundation can still be discussed.

[42] The spatial pattern of flooded area in FLD+Diff (Figure 8b) was well reproduced when compared with satellite observations (Figure 8a). The expansion of flooded areas in high-water season was predicted along the mainstream and the Purus River. The flooded area simulated by the model was noisier than the satellite observation, probably because of the errors in input DEM which cannot be removed by the correction algorithm explained in Appendix B. The total flooded areas in high (low) water season were 213,500 km^2 (92,300 km^2) for the satellite observation, 214,300 km^2 (93,900 km^2) for FLD+Diff, and 202,500 km^2 (96,600 km^2) for FLD+Kine.

[43] General patterns of flooded area were similar between FLD+Diff and FLD+Kine, but the flooded area along streamlines was narrower in FLD+Kine compared with FLD+Diff and observation (Figure 8). Even though flooding in the grid points that represented the mainstream and major branches was predicted by FLD+Kine, inundation did not expand to surrounding grid points around these streams. The correlations of flooded fraction in every grid cell within Figure 8 were calculated between the model and the satellite observation. The correlation coefficients were higher in FLD+Diff (0.64 for high-water and 0.43 for low water) than FLD+Kine (0.51 for high-water and 0.31 for low water). Even though the total flooded areas within the domain of Figure 8 were similar in FLD+Diff and FLD+Kine, higher correlation coefficients by FLD+Diff indicate that the diffusive wave approximation is a better way for representing floodplain inundation dynamics than the kinematic wave approximation.

[44] The time series of total flooded area within the central Amazonian floodplains (from 0°S–54°W to 8°S–72°W, the area of Figure 8) from 1993 through 2000 is illustrated in Figure 9. The thick gray line represents the multisatellite observation by *Prigent et al.* [2007], and the while lines with circles and squares represent the simulations by FLD+Diff and FLD+Kine, respectively. The multisatellite data set by Prigent el al. was prepared in equal-area projection, so it was linearly interpolated to the longitude-latitude-based rectangular coordinate system at the 15 arc min resolution. The multisatellite estimate was used for validating the temporal variation of flooded area because the high-resolution SAR images by *Hess et al.* [2003] were available only for the two snapshots shown in Figure 8.

[45] It is found that the amplitude of the seasonal cycle was larger in the model than the multisatellite estimation. This is because the multisatellite observation underestimates the true amount of flooded area owing to limitations on detecting small flooded areas by microwave imager [*Prigent et al.*, 2007]. When the simulated flooded area was compared to the more accurate estimation by SAR imaging [*Hess et al.*, 2003] (the pluses in Figure 9), the amplitudes of seasonal flooding became similar between simulation and observation.

[46] Instead, discussion on the phase of the seasonal cycle can be made because multisatellite estimation is available at the monthly time scale. The correlation coefficients between multisatellite estimation and simulation were 0.69 and 0.67 for FLD+Diff and FLD+Kine, respectively. It is also found from Figure 9 that the peak of flooding was about 1 month earlier in the model than the multisatellite observation. This is probably due to the assumption of the instantaneous exchange of water between river channels and floodplains in CaMa-Flood. It is known from observation that the water surface elevations are not equal between river channels and floodplains [*Alsdorf et al.*, 2005]. Hence, it is possible that
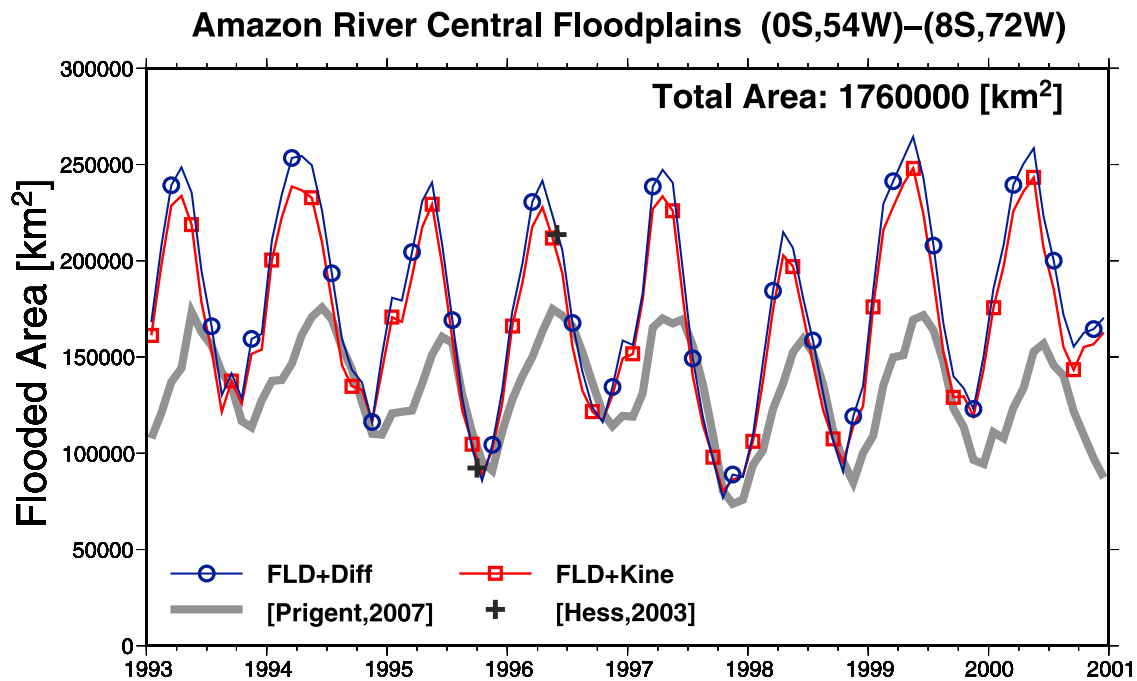
Figure 9. Monthly averaged flooded area within the central Amazonian floodplains (from 0°S–54°W to 8°S–72°W, area of Figure 8). Thick gray line is multisatellite observation. The lines marked with circles and squares indicate simulation by FLD+Diff and FLD+Kine, respectively.

water level change in floodplains is delayed from that in river channels.

5.2. Major World River Basins

[47] The 30 major basins in Table 2 were selected for the validation of CaMa-Flood according to the availability of daily river discharge data from the GRDC. The gauging station located farthest downstream in each basin was used for validation of the model's ability as a global-scale river routing model. The longitude and latitude of the gauging stations, upstream drainage area (10^3 km^2), and years used for validation are listed. Annual averaged discharge (m^3/s) for observation, Q_{obs}, and simulation, Q_{sim}, are shown. The correlation coefficient, R, and Nash-Sutcliffe's modeling efficiency, ME, between observation and simulation were calculated. Daily river discharges for all gauging stations are given in Table 2, and two are illustrated in Figure 10. The thick gray line indicates observed river discharge provided by GRDC. The lines marked with circles, squares, and triangles indicate simulated discharge by FLD+Diff, FLD+Kine, and NoFLD, respectively.

[48] For all the rivers in Table 2, ME was better in the experiments with a floodplain reservoir (FLD+Diff and FLD+Kine) than the experiment without it (NoFLD). As shown in Figure 10, flood peak discharge was mostly overestimated in NoFLD because water levels increase too much in a rectangular river channel without a floodplain reservoir. On the other hand, the fluctuation of water level was suppressed in simulations with floodplain reservoirs because floodplains store water during flooding; hence, simulated flood peak discharge was smaller in FLD+Diff and FLD+Kine. Correlation coefficients were also higher or similar in the simulation with flooding scheme (FLD+Diff

and FLD+Kine) than in the simulation without it (NoFLD) except for the Don River, where the error in input runoff was large.

[49] Even though improvement by introducing floodplains was observed in most of the rivers, MEs for FLD+Diff and FLD+Kine were still negative in some gauging stations, which suggests large disagreement between simulated and observed river discharge. However, it is found that the discussion on river discharge using ME is not suitable in some rivers such as the St. Lawrence River and the Neva River, whose gauging stations are located on the downstream of huge lakes. Daily river discharges in those rivers were not sensitive to input runoff because water levels stay almost constant because of the existence of a large lake (see Figure 10). Even though ME was negative, significant improvement in simulated river discharge by introducing the flooding scheme was observed in Figure 10. Because the flat surface of a lake was represented in the floodplain elevation profile, the constant water level was predicted in CaMa-Flood even though the topographic depression of the lake was not considered.

[50] The other rivers with negative ME might be affected by external causes out of the model's framework, such as dam operation or unrealistic input runoff from LSM. Daily river discharges in the Columbia River and the Nelson River are affected by dam operation because unnatural high-frequency oscillations were observed in the gauged river discharge (see Figure 10). The relative errors larger than 50% in the Congo, Volga, Ubangi, Dniepr, Chari, Don, and Syr-Darya suggested large uncertainty existing in input runoff. Given that input runoff from LSM was not realistic in those basins, simulation of river discharge must be worse than in the basins with realistic input runoff.

Table 2. Summary of Daily River Discharge in Major World Basins[a]

Basin	Station	Longitude	Latitude	Area	Year	Q_{obs}	Q_{sim}	FLD+Diff		FLD+Kine		NoFLD	
								R	ME	R	ME	R	ME
Amazonas	Obidos	−55.50	−1.90	4640	1993–1995	177759.8	194379.2	0.97	0.83	0.95	0.78	0.35	−1.93
Congo	Kinshasa	15.30	−4.30	3475	1981–1983	37688.9	70691.8	0.61	−14.68	0.67	−14.14	0.22	−23.65
Orinoco	Puente Angostura	−63.60	8.15	836	1987–1989	30241.4	30169.2	0.93	0.85	0.94	0.87	0.65	−0.08
Brahmaputra	Bahadurabad	89.67	25.18	636	1989–1991	27014.9	17832.9	0.91	0.62	0.91	0.63	0.77	0.30
Yenisei	Igarka	86.50	67.48	2440	1997–1999	19670.3	13308.8	0.82	0.61	0.72	0.38	0.75	0.32
Mississippi	Vicksburg, MS	−90.91	32.31	2964	1995–1997	17896.8	20296.0	0.84	0.41	0.83	0.45	0.63	−1.92
Lena	Stolb	126.80	72.37	2460	1992–1994	15570.3	11861.6	0.88	0.72	0.78	0.52	0.55	−0.45
Ob	Salekhard	66.53	66.57	2949	1997–1999	13810.2	15977.9	0.94	0.80	0.89	0.66	0.09	−6.94
Mekong	Stung Treng	105.94	13.53	635	1992–1994	12893.5	11335.2	0.97	0.94	0.97	0.92	0.87	0.65
Amur	Komsomolsk	137.12	50.63	1730	1988–1990	11614.5	9725.5	0.92	0.76	0.88	0.71	0.40	−1.03
Irrawaddy	Sagaing	96.10	21.98	117	1986–1988	8438.6	4543.5	0.88	0.48	0.88	0.47	0.71	0.17
Mackenzie	Arctic Red River	−133.74	67.46	1660	1994–1996	8088.1	8681.5	0.83	0.04	0.89	0.42	0.53	−6.86
Volga	Volgograd	44.72	48.77	1360	1988–1990	7985.2	12270.4	0.87	−4.80	0.80	−4.25	0.60	−19.79
St. Lawrence	Cornwall	−74.80	45.01	774	1991–1993	7730.4	5609.1	0.64	−5.59	0.63	−3.66	0.15	−58.40
Yukon	Pilot Station, AK	−162.88	61.93	831	1993–1995	6813.6	4621.4	0.81	0.48	0.69	0.13	0.34	−2.14
Uruguay	Salto	−57.93	−31.38	244	1992–1994	6354.0	7349.7	0.63	0.29	0.51	0.11	0.52	−1.65
Danube	Lom	23.24	43.84	588	1997–1999	5932.7	6096.1	0.66	0.42	0.64	0.39	0.53	−5.29
Columbia	The Dalles, OR	−121.17	45.61	613	1998–2000	5466.6	3539.2	0.80	−1.13	0.81	−0.96	0.63	−2.69
Pechora	Oksino	52.18	67.63	312	1996–1998	4978.9	3590.6	0.75	0.48	0.62	0.33	0.70	0.23
Kolyma	Kolymskaya	158.72	68.73	526	1996–1998	3637.0	2463.8	0.83	0.62	0.69	0.44	0.41	−1.17
Northern Dvina	Ust. Pinega	42.17	64.10	348	1996–1998	3290.0	3410.8	0.91	0.82	0.88	0.77	0.70	−1.00
Nelson	Long Spruce	−94.37	56.40	1060	1998–2000	3281.1	3699.6	0.05	−10.20	0.05	−11.20	−0.05	−122.90
Ubangi	Bangui	18.58	4.37	500	1991–1993	2918.4	8675.6	0.91	−13.83	0.92	−13.60	0.73	−18.49
Neva	Novosaratovka	30.72	59.80	281	1986–1988	2567.3	3051.1	0.43	−0.40	−0.20	−0.92	0.37	−56.56
Rhine	Lobith	6.11	51.84	160	1998–2000	2533.3	2696.6	0.71	0.19	0.69	0.22	0.55	−3.54
Amu Darya	Kerki	65.25	37.83	309	1987–1989	1345.0	1720.6	0.49	−2.31	0.49	−2.39	0.36	−4.70
Dniepr	Kakhovskaya Ges	33.18	46.82	482	1986–1988	1300.6	2993.8	0.30	−13.42	0.26	−13.00	0.05	−73.19
Chari	Ndjamena	15.03	12.12	600	1988–1990	591.0	1265.9	0.62	−2.75	0.56	−3.28	0.60	−10.08
Don	Razdorskaya	40.67	47.50	378	1988–1990	564.8	1819.1	−0.06	−231.71	−0.10	−184.13	0.21	−549.69
Syr Darya	Tyumen Aryk	67.05	44.05	219	1984–1986	180.6	899.1	0.64	−62.75	0.65	−65.92	0.00	−144.70

[a]R, correlation coefficient; Q_{obs}, annual averaged discharge for observation; Q_{sim}, annual averaged discharge for simulation; ME, Nash-Sutcliffe modeling efficiency.

[51] When rivers with negative MEs were excluded, correlation coefficients and MEs were generally similar or better in FLD+Diff than those in FLD+Kine. This result indicates that flow computation by the diffusive wave equation was effective for decreasing errors in simulated daily river discharge in the mainstreams of the world's major rivers. This is probably true because the mainstreams of most major river basins are located in flat regions where a backwater effect occurs and the gauging stations that are the farthest downstream were chosen for the validation of daily river discharge.

[52] Most of the gauging stations with relatively low ME (<0.5) were probably affected by the errors in estimated channel width and bank height. Those parameters were considered to be underestimated in the Mississippi, Uruguay, Danube, Pechora, and Rhine because the fluctuations of daily river discharge were larger in observations than the model simulations with floodplain storages. On the other hand, they were likely to be overestimated in the Mackenzie River because the flood peak discharge was overestimated by the mode. As discussed in section 6, the fluctuation of daily river discharge becomes smaller (larger) when river channel is narrower (wider) or bank height is shallower (deeper). Those errors might be reduced if parameters for river channel and bank height are tuned for each river instead of using the identical empirical equations for river channel and bank height globally.

[53] Figure 11 illustrates the annual maximum flooded area fraction averaged from 1993 to 2000. The simulated result by FLD+Diff is shown in Figure 11a, while the multisatellite observation [*Prigent et al.*, 2007] is shown in Figure 11b. Lake surface areas from the Global Lake and Wetland Database [*Lehner and Döll*, 2004] were overlapped to the multisatellite observation because large lakes were masked and were not represented in the data sets of *Prigent et al.* [2007]. Note that high-water channels and small backwater lakes are treated as "floodplains" within the framework of CaMa-Flood, so that inundations in those reservoirs are also represented as flooded area in Figure 11.

[54] CaMa-Flood reproduced floodplain inundations along the mainstreams of major rivers, such as the Amazon, Parana, Mississippi, Ob, Lena, and Ganges. However, the inundated area was generally underestimated by FLD+Diff compared with observation. Underestimated inundation in northern Canada, the Scandinavian peninsula, and western Siberia were due to small topographic depressions, which are not connected to river channels [*Pavelsky and Smith*, 2008a]. As the mechanism of inundation in local depressions is different from that of floodplains along river channels, it cannot be predicted within the framework of CaMa-Flood. Similarly, inundation in irrigated paddy fields observed in southern and southeastern Asia [*Matthews et al.*, 1991] is out of the remit of CaMa-Flood. Therefore, the underestimation of inundated area by FLD+Diff was within the range of expectation, and inundation in floodplains along major rivers was appropriately reproduced in CaMa-Flood.

[55] Time series of monthly flooded area averaged from 1993 to 2000 is illustrated in Figure 12. The results for the
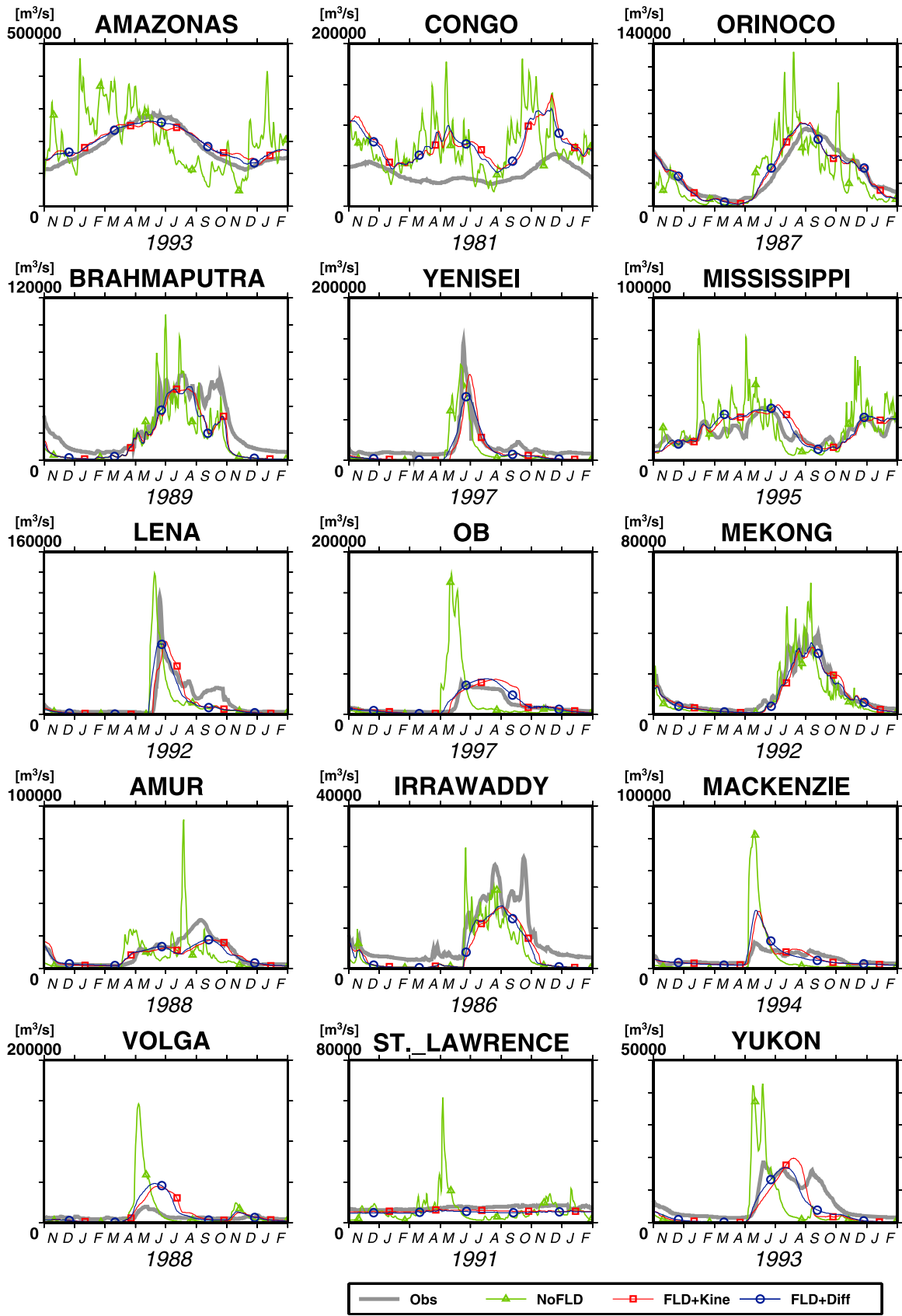
Figure 10. Daily discharge in major rivers. Thick gray line represents observation by GRDC. The lines marked with circles, squares, and triangles indicate simulation by FLD+Diff, FLD+Kine, and NoFLD, respectively.
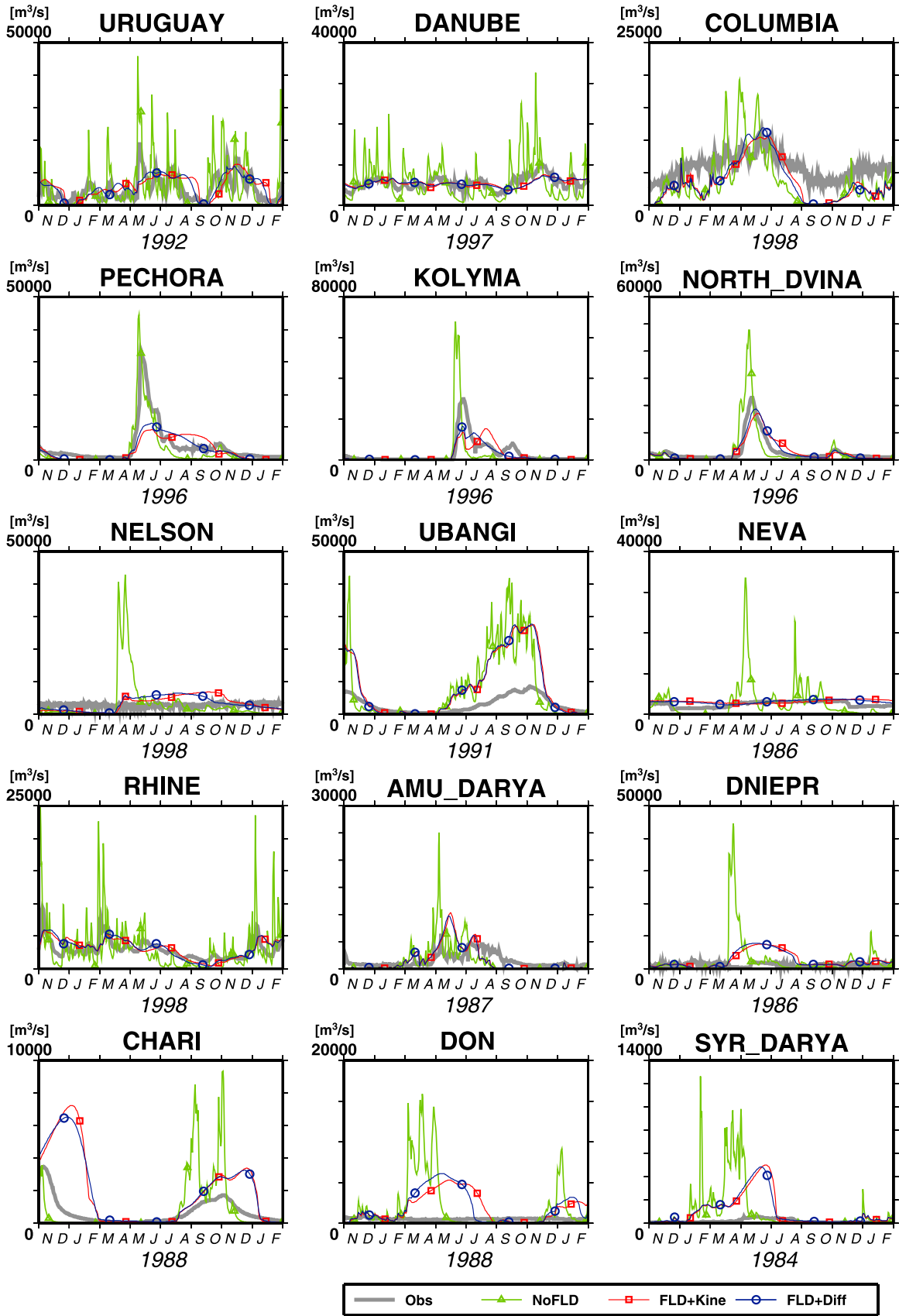
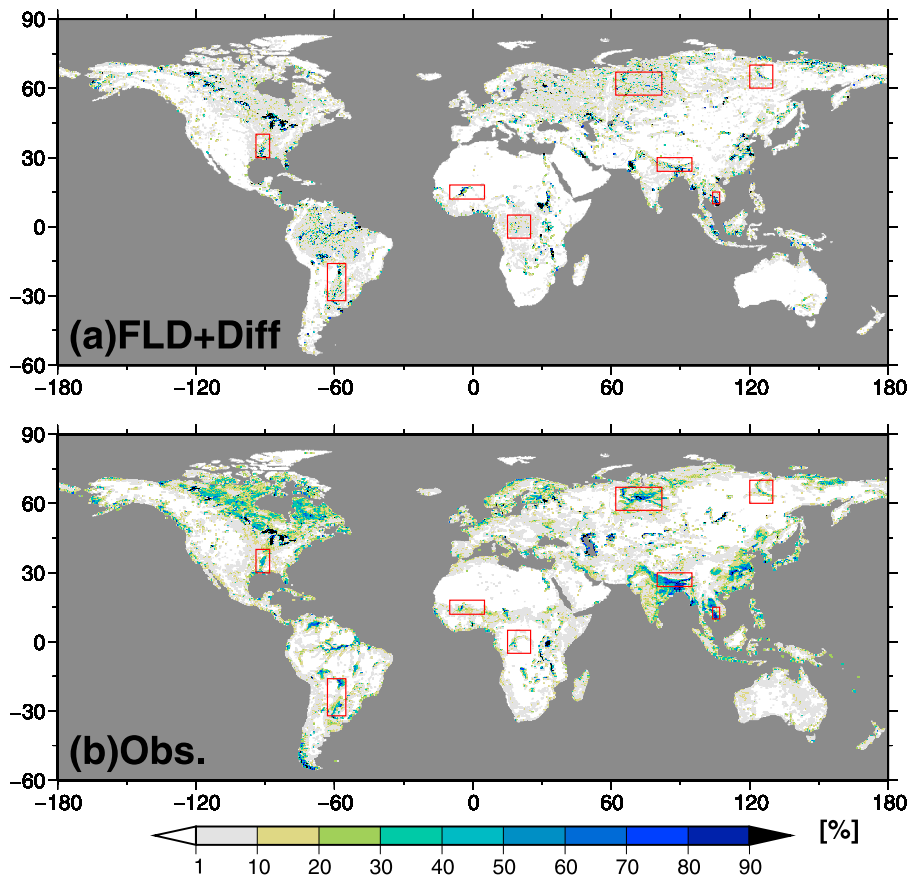**Figure 10.** (continued)

Figure 11. Annual maximum flooded area fraction averaged from 1993 to 2000. (a) FLD+Diff simulation and (b) satellite observation. The red squares indicate the regions used for the validation of flooded area in Figure 12.
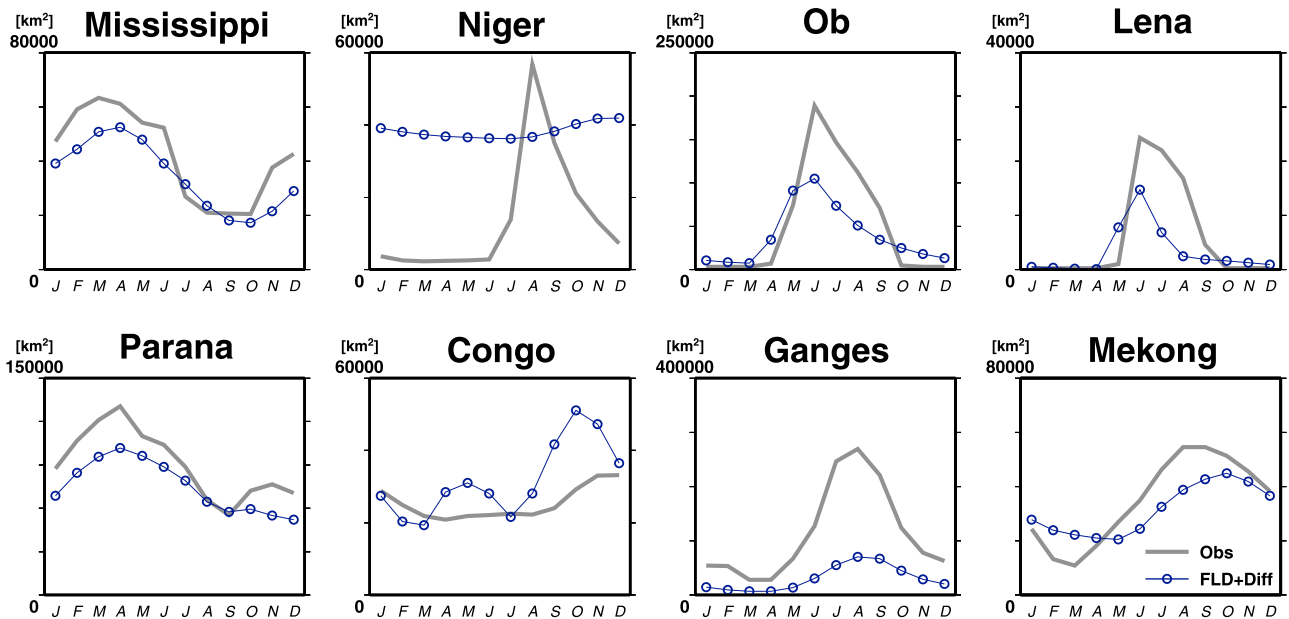

Figure 12. Monthly flooded area averaged from 1993 to 2000. The regions indicated by red squares in Figure 11 are shown. Thick gray line is multisatellite observation, while the line marked with circles represents FLD+Diff.

Table 3. Summary of Monthly Flooded Area for World Major Basins

Basin	Domain	A_{obs}	A_{sim}	RE	R
Mississippi	(40°N, 88°W) to (30°N, 94°W)	43,200	34,500	−0.25	0.92
Parana	(16°S, 63°W) to (32°S, 55°W)	90,700	75,200	−0.21	0.94
Niger	(18°N, 10°W) to (12°N, 5°E)	13,600	38,300	0.64	−0.05
Congo	(5°N, 15°E) to (5°S, 25°E)	25,400	31,700	0.20	0.63
Ob	(67°N, 62°E) to (57°N, 82°E)	51,700	39,300	−0.32	0.88
Ganges	(30°N, 80°E) to (24°N, 95°E)	113,100	30,600	−2.70	0.96
Lena	(70°N, 120°E) to (60°N, 130°E)	5,900	3,200	−0.84	0.75
Mekong	(15°N, 104°E) to (10°N, 107°E)	34,900	31,400	−0.11	0.87

Mississippi, Parana, Niger, Congo, Ob, Ganges, Lena, and Mekong basins are shown (see red squares in Figure 11). The thick gray line indicates the multisatellite estimation of flooded area by *Prigent et al.* [2007], while the line with circles indicates the simulated result by the FLD+Diff experiment. The average of flooded area within each domain (A_{obs} for observation and A_{sim} for simulation), relative error of flooded area, RE, and the correlation coefficient between the observation and the model simulation, R, are summarized in Table 3.

[56] The seasonal cycle of the flooded area was well reproduced in the Mississippi, Parana, and Mekong compared to the other basins. This is probably because floodplains and wetlands in those basins are mainly fed by flooding from river channels, while flooded areas in other basins are affected by processes which were not considered in the model. For example, northern rivers like the Ob and Lena have many small lakes which are not strongly connected to river channels [*Pavelsky and Smith, 2008a*]. The Ganges basin is largely affected by irrigated paddy fields [*Matthews et al.*, 1991], which were observed by the satellites but are not represented in the model. The overestimation of flooded area in the Niger River was probably due to infiltration and evaporation from floodplains, which are not negligible in the arid basin [*Sellars*, 1981] but are neglected in CaMa-Flood. Further studies for quantifying the impact on flooded area by the processes outside of the model are required, while reduction of the uncertainties within the model such as channel width or bank height is also essential.

6. Sensitivity to Parameters

[57] Most of the parameters in CaMa-Flood (see Table 1) were objectively derived from the 1 km resolution DEM using the FLOW method [*Yamazaki et al.*, 2009], while three of them (i.e., river channel width, bank height, and Manning's roughness coefficient) ware empirically decided. River channel width and bank height were given as the function of monthly based discharge as written in equations (10) and (11). The Manning's roughness coefficient was assumed to be constant.

[58] Those empirical parameters were assumed to be identical for all the basins in order to execute global simulations because observations for parameter calibration are not enough in many basins. However, the bathymetry of river channel and the roughness coefficient must vary for each basin (or each subbasin) according to geomorphologic conditions (e.g., slope and curvature) and geological conditions (e.g., sediment type and grain size) [*Leopold and Maddock*, 1953]. The extensive calibration of the bathymetric parameters and the roughness coefficient for each

basin was not performed in this study. Instead, the model's sensitivity to those parameters was tested.

[59] The sensitivities of CaMa-Flood to river channel width, bank height, and Manning's roughness coefficient were checked by perturbing those parameters. The experiment using the same parameters as the FLD+Diff experiment was named CTL in the sensitivity test. The experiments that perturbed river channel width by −50%, −20%, +20%, and +50% were termed W−50, W−20, W+20, and W+50, respectively. The experiments that perturbed bank height by −50%, −20%, +20%, and +50% were similarly termed B−50, B−20, B+20, and B+50, respectively. The experiments that changed Manning's roughness coefficient by −50% ($n = 0.015$), −20% ($n = 0.024$), +20% (n = 0.036), and +50% ($n = 0.045$) were named M−50, M−20, M+20, and M+50, respectively. For each experiment, only one parameter was perturbed, and the other two parameters were set to the same value as CTL. Simulations were executed from 1992 to 1994. The year 1992 was discarded for spin-up, and the results for the other 2 years were analyzed.

[60] Figures 13 and 14 illustrate the simulated daily river discharge (top) and flooded area (bottom) for the Amazon River and the Ob River, respectively. The gauging stations for discharge and the domains for calculating flooded area were the same as those used for the validation of the FLD+Diff experiment. The results of perturbing bank height, channel width, and Manning's roughness coefficient are shown in Figure 13 (right, middle and left, respectively) and Figure 14 (right, middle and left, respectively). In situ gauged river discharge from GRDC and satellite estimation of flooded area [*Prigent et al.*, 2007] are also shown in Figures 13 and 14.

[61] For both basins, the fluctuation of simulated discharge became larger (smaller) when bank height was deeper (shallower), channel width was wider (narrower), or Manning's roughness coefficient was smaller (larger). This is because flooding from river channels happens more easily when bank height is shallower, channel width is narrower, or the roughness coefficient is larger. According to equation (7) for flow velocity estimation, river flow velocity gets slower with a narrower channel or larger roughness coefficient, so that water tends to be stored within channels and floodplain reservoirs rather than being discharged into a downstream grid. Because water level becomes less sensitive to storage change when the flooded area becomes larger, the fluctuation of river discharge was suppressed in the simulation with shallow bank height, wide river channel, or large roughness coefficient.

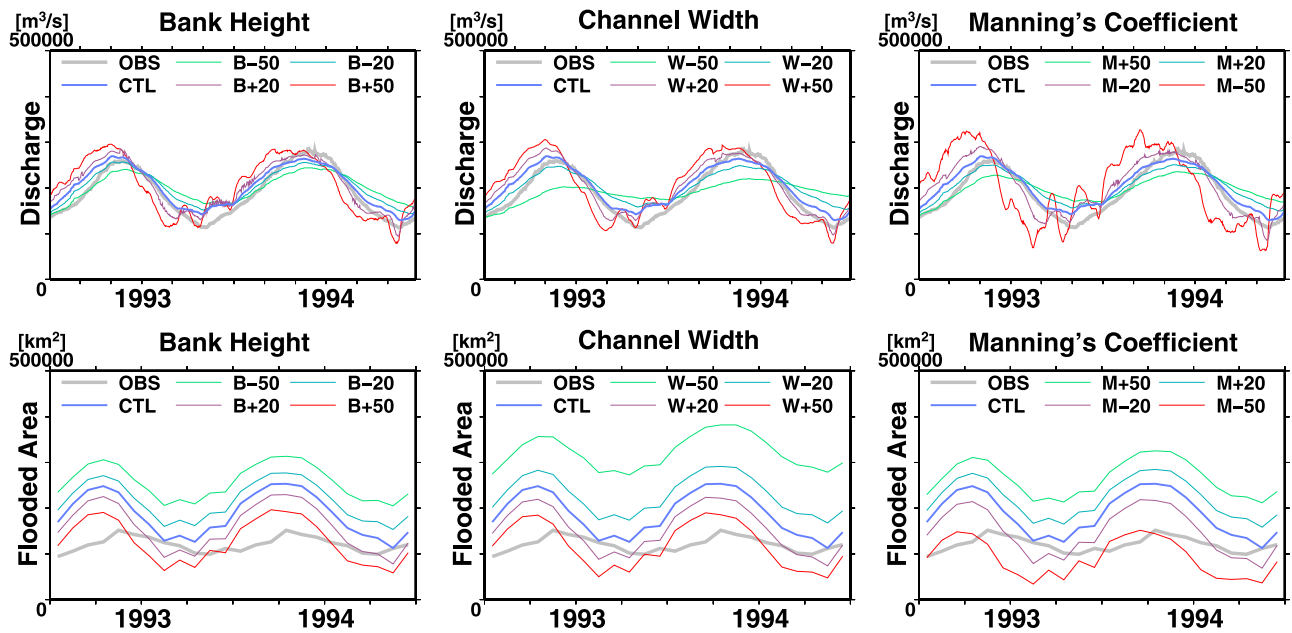[62] The timing of flood peak was delayed (advanced) in the simulation with shallow (deep) bank height, narrow

Figure 13. Sensitivity of (top) simulated river discharge and (bottom) flooded area to (left) bank height, (middle) river channel, and (right) Manning's roughness coefficient for the Amazon River. Observed values of river discharge and flooded area are shown by the thick gray line, while simulated results by perturbing parameters are shown by the color lines.

(wide) channel or large (small) roughness coefficient. The delay of flood peaks is also explained with the impact of floodplain storages. According to the mass conservation equation (9), water level (or water storage in a grid) increases until the inflows and outflow from of a grid reach equilibrium. Because water level increase is slower when the flooded area becomes larger, it takes longer for the inflows and outflow to reach the equilibrium state in the simulation with shallower bank height, narrower river channel, or larger roughness coefficient.

7. Summary and Discussion

[63] Floodplain inundation dynamics along the mainstreams of major river basins is represented in the Catchment-Based Macro-scale Floodplain (CaMa-Flood) model. Explicit
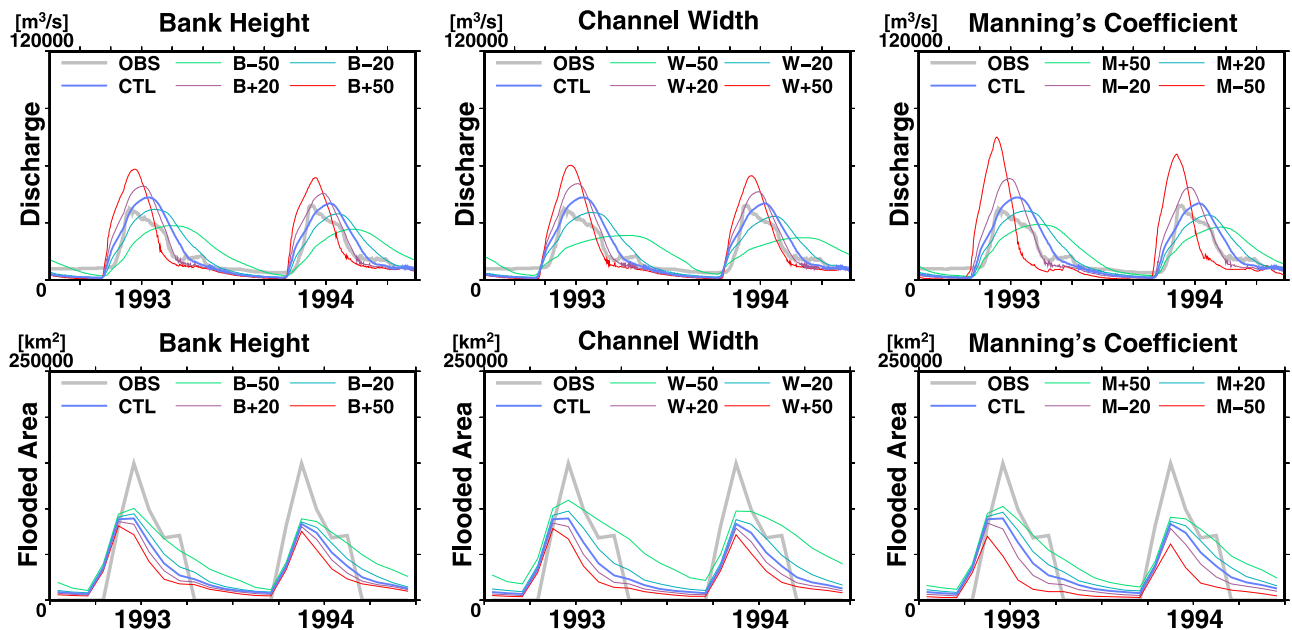

Figure 14. Same as Figure 13 but for the Ob River.

predictions of inundated area and water level in floodplains were achieved by the description of floodplain elevation profiles based on 1 km resolution hydrotopographical data sets. The relationship between the storage and stage of surface water was decided from the 1 km resolution DEM in a physically based manner. Consideration of backwater effect was also incorporated in CaMa-Flood by adapting the diffusive wave equation. The simulation of daily river discharge was improved in most of world's major rivers by introducing subgrid floodplain topography. The smooth profile of water surface elevation along the river networks was represented when the diffusive wave equation was used for the governing equation of river flow. Simulated inundation in floodplains along major rivers agreed well with satellite observations.

[64] However, various points still need to be improved. For example, the SRTM30 DEM used to define topographic parameters of CaMa-Flood still has large uncertainty; even though this DEM has a sufficient resolution, the accuracy is not adequate to describe the relationship among water storage, water level, and inundated area. A satellite-derived DEM has an uncertainty due to vegetation canopy [*Sun et al.*, 2003], so it may not represent the actual terrain surface on which floodplains are formed. A technique for deriving the actual terrain surface from a DEM is required for more precise simulation of floodplain inundation dynamics.

[65] Uncertainty in other topographic parameters should also be considered. River channel width and bank height were defined as an empirical function of annual river discharge in this study. Those parameters are quite important because they decide the capacity of a river channel to hold water during flooding. We used the identical empirical equation for all basins in order to validate the ability of CaMa-Flood as a global-scale mode, but it would be better for calibrating these parameters for each basin when we apply the model for water resources studies. In situ observed discharge required for calibration of parameters is generally limited in many rivers, but calibration of the parameters using satellite data sets such as inundated area would be a possible topic for future studies. Furthermore, some recent studies have begun to determine channel width and water depth using satellite observations [e.g., *Pavelsky and Smith*, 2008b; *Durand et al.*, 2008], and corroboration with those techniques is a challenging task. To reduce the uncertainty in CaMa-Flood, we need to incorporate these parameter estimation methods.

[66] Some drawbacks were found in the assumptions of CaMa-Flood. First, an increasing function was assumed to describe a floodplain inundation profile, but local depression in floodplains must also be considered. This was the main reason for the underestimation of inundated areas in northern regions, as shown in Figures 11 and 12, where numbers of small pools are formed in local depressions [*Matthews and Fung*, 1987]. Furthermore, all topographic depressions that include permanent lakes and wetlands were treated as floodplains by this assumption, but it would be better to distinguish the lakes and wetlands from floodplains in future works. Second, artificial regulation of water resources was not assumed in CaMa-Flood, even though actual river flow is highly affected by human activities. The impact of dams and irrigation should be considered for a more realistic simulation of river flow [e.g., *Hanasaki et al.*, 2008]. Irri-

gated paddy fields must also be modeled to predict variations in inundated areas, as they are noticeable on a global scale [*Matthews et al.*, 1991]. Third, water exchange between river channels and floodplains within the subgrid scale was assumed to be instantaneous in this study. However, the movement of water between river channels and floodplains is known to be more complex [*Alsdorf et al.*, 2005, 2007]. Consideration of the detailed physics of floodplain infilling and draining would be required for further improvement of the proposed model.

[67] Interaction between surface water and other hydrospheres was not treated in CaMa-Flood. In this study, input runoff was externally calculated by a land surface model, so the interaction between surface water and subsurface water was not considered. Because the generation of subsurface runoff is affected by the surface water table [*Sophocleous*, 2002], dynamic coupling of a surface water model and a land surface model will be important. Infiltration from river to soil must be a major source of soil moisture in arid and semiarid regions [*Wolski et al.*, 2006], and this was also not considered in CaMa-Flood. Moisture flux from surface waters to the atmosphere was also neglected in this study, which may have a significant impact on both regional climate [*Krinner*, 2003] and land hydrology [*Sellars*, 1981].

[68] Despite the limitations discussed above, the global-scale prediction of inundated area and water level achieved by CaMa-Flood is quite important. Assessment of water resources and flood hazards will be enhanced by utilizing information on water stages as well as daily river discharge. Incorporating the proposed method into climate models is also interesting because the prediction of water surface area may have an impact on the atmosphere. Ongoing research will entail the application of CaMa-Flood to various hydrological problems, though further improvement of the model is also required.

Appendix A: Detailed Method for Flow Computation

[69] The diffusive wave equation, which solves river discharge on the basis of water surface elevation in upstream and downstream grid points, is generally unstable for numerical computation. To suppress numerical oscillation, a leapfrog-type method is used in CaMa-Flood. Here, water storage in time step $t + \Delta t$ is calculated by utilizing information from intermediate time step $t + \Delta t/2$ rather than from time step t. River discharge at time step $t + \Delta t/2$ is defined as follows:

$$Q_i^{t+\Delta t/2} = \frac{1}{2}\left(\widetilde{Q}_i^{t+\Delta t/2} + Q_i^t\right), \quad (A1)$$

where Q_i^t is the "actual" river discharge at grid point i at time step t and is used for predicting water storage in future time step $t + \Delta t/2$. $\widetilde{Q}_i^{t+\Delta t/2}$ is "temporary" river discharge estimated by the diffusive wave equation using water storage at time step $t + \Delta t/2$. Hence, actual river discharge for predicting water storage in the next time step is given as the average of temporary river discharge estimated at the current time step and actual river discharge at the previous time step.
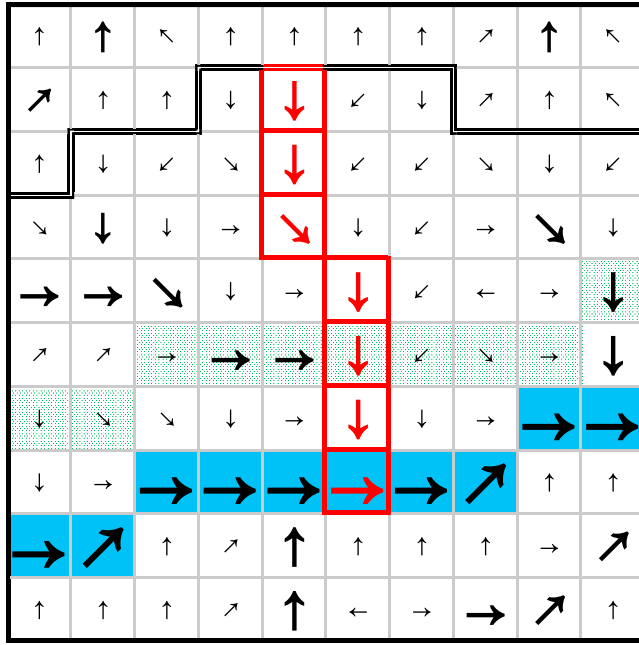
Figure B1. An example for a positioning error of river channels in the flow direction map. The flow direction for each pixel is represented by a vector. River channel pixels from the flow direction map and from the DEM are shaded and dotted, respectively. A streamline on which elevations are modified by the sorting algorithm is enhanced by thick red borders.

[70] By this definition, water storage at time steps $t + \Delta t/2$ and $t + \Delta t$ are derived as follows:

$$S_i^{t+\Delta t/2} = S_i^t + \frac{1}{2}\left(Q_{\text{net}}^t + A_{c_i}R_i^t\right)\Delta t \qquad (A2)$$

$$S_i^{t+\Delta t} = S_i^{t+\Delta t/2} + \frac{1}{2}\left(Q_{\text{net}}^{t+\Delta t/2} + A_{c_i}R_i^t\right)\Delta t, \qquad (A3)$$

where Q_{net}^t is net river discharge (i.e., inflow from upstream minus outflow toward downstream) of the grid point i at time step t:

$$Q_{\text{net}}^t = \sum_k^{\text{upstream}} Q_k^t - Q_i^t. \qquad (A4)$$

Substituting (A1) and (A2) into (A3) yields

$$S_i^{t+\Delta t} = S_i^t + \left(\frac{3}{4}Q_{\text{net}}^t + \frac{1}{4}\widetilde{Q}_{\text{net}}^{t+\Delta t/2}\right)\Delta t + A_{c_i}R_i^t\Delta t. \qquad (A5)$$

Because net river discharge between time steps $t + \Delta t$ and t is calculated using water storage at intermediate time step $t + \Delta t/2$, numerical instability is reduced compared to when it is calculated only from water storage at time step t.

[71] In addition, estimated river discharge should be modified when total outflow from one grid point exceeds water storage of that grid point in order to conserve water mass. Water is drained from upstream grid points when flow is toward downstream, whereas it is drained from down-

stream grid points when flow is backward. Hence, total outflow, O_i, from grid point i is calculated as follows:

$$O_i = \sum_k^{\text{upstream}}(1 - \beta_k)Q_k\Delta t + \beta_i Q_i\Delta t, \qquad (A6)$$

where β_i is an indicator of flow direction at grid point i. $\beta_i = 1$ when flow is toward downstream, whereas $\beta_i = 0$ when reverse flow occurs.

[72] If total water outflow exceeds water storage, the modified discharge at grid point i is calculated as follows:

$$\dot{Q}_i = \left(\beta_i r_i + (1 - \beta_i)r_j\right)Q_i \qquad (A7)$$

$$r_i = \max[1, O_i/S_i], \qquad (A8)$$

where $\dot{Q}_i$ is modified river discharge, Q_i is originally calculated river discharge, r_i is the modification rate, and S_i is water storage. Index j indicates the downstream grid point of grid point i. Therefore, the modification rate of grid point i is applied when flow is toward downstream, whereas that of downstream grid point j is applied when flow is toward upstream. By applying this modification to discharge originally calculated by equation (A1), conservation of water mass is achieved.

Appendix B: Correction of Surface Elevation Map

[73] The surface elevation map was created by interpolating SRTM30 DEM onto the GDBD flow direction map. However, because of the uncertainty in satellite-based observation and the discrepancy in stream positions between GDBD and SRTM30, negative topographic slopes (i.e., downstream elevation is higher than upstream elevation) were found in the interpolated surface elevation map. Those negative slopes were removed by applying the following correction algorithm.

[74] First, the negative slopes due to the positioning error of river channels were removed. Because the flow direction map of GDBD was generated from the GTOPO30 DEM [*Masutomi et al.*, 2009], the positions of river channels represented in GDBD and SRTM30 were possibly different. As shown in Figure B1, the elevations of river pixels considered to represent river channels in SRTM30 (dotted pixels) are expected to be lower than the elevations of river channel pixels in GDBD (shaded pixels). In order to represent the elevation of river channel pixels realistically, a sorting algorithm for a streamline from a hilltop pixel to a river channel pixel (pixels with thick red borders) was performed. Here, pixels with more than 100 upstream grids were considered to be river channel pixels. The elevations of pixels in the streamline were sorted to satisfy the condition that downstream is always lower than upstream. The positions of river channels in the flow direction map and the DEM become the same by applying this sorting algorithm for every streamline found in the flow direction map.

[75] Second, the elevation of each pixel was replaced by the average of the elevation within the river segment 5 km upstream or downstream from the pixel under consideration. The averaged elevation of the river segment was adapted to cancel high-frequency noises in a satellite-derived DEM [*Rodriguez et al.*, 2006]. Then negative slopes were

removed along each river stream by lowering (or lifting) the elevation of the downstream (or upstream) pixel where a negative slope was found. Whether elevation is lowered or lifted was chosen to minimize the required amount of modification on the DEM. This procedure is effective for removing long-wavelength errors mainly due to tilts in the spacecraft maneuver [*Rodriguez et al.*, 2006].

References

Alsdorf, D. E., J. M. Melack, T. Dunne, L. A. K. Mertes, L. L. Hess, and L. C. Smith (2000), Interferometric radar measurements of water level changes on the Amazon flood plain, *Nature*, *404*, 174–177, doi:10.1038/35004560.

Alsdorf, D., T. Dunne, J. Melack, L. Smith, and L. Hess (2005), Diffusion modeling of recessional flow on central Amazonian floodplains, *Geophys. Res. Lett.*, *32*, L21405, doi:10.1029/2005GL024412.

Alsdorf, D. E., P. D. Bates, J. M. Melack, M. D. Wilson, and T. Dunne (2007), The spatial and temporal complexity of the Amazon flood measured from space, *Geophys. Res. Lett.*, *34*, L08402, doi:10.1029/2007GL029447.

Alsdorf, D., S.-C. Han, P. Bates, and J. Melack (2010), Seasonal water storage on the Amazon floodplain measured from satellites, *Remote Sens. Environ.*, *114*, 2448–2456, doi:10.1016/j.rse.2010.05.020.

Andreadis, K. M., E. A. Clark, D. P. Lettenmaier, and D. E. Alsdorf (2007), Prospects for river discharge and depth estimation through assimilation of swath altimetry into a raster-based hydrodynamics model, *Geophys. Res. Lett.*, *34*, L10403, doi:10.1029/2007GL029721.

Bates, P. D. (2000), Development and testing of a sub-grid scale model for moving boundary hydrodynamic problems in shallow water, *Hydrol. Processes*, *14*, 2073–2088, doi:10.1002/1099-1085(20000815/30) 14:11/12<2073::AID-HYP55>3.0.CO;2-X.

Bates, P. D., and A. P. De Roo (2000), A simple raster-based model for flood inundation simulation, *J. Hydrol.*, *236*, 54–77, doi:10.1016/S0022-1694(00)00278-X.

Biancamaria, S., P. D. Bates, A. Boone, and N. M. Mognard (2009), Large-scale coupled hydrologic and hydraulic modelling of an arctic river: The Ob River in Siberia, *J. Hydrol.*, *379*, 136–150, doi:10.1016/j.jhydrol.2009.09.054.

Coe, M. T., and G. B. Bonan (1997), Feedbacks between climate and surface water in northern Africa during the middle Holocene, *J. Geophys. Res.*, *102*(D10), 11,087–11,101, doi:10.1029/97JD00343.

Coe, M. T., M. H. Costa, A. Botta, and C. Birkett (2002), Long-term simulation of discharge and floods in the Amazon basin, *J. Geophys. Res.*, *107*(D20), 8044, doi:10.1029/2001JD000740.

Coe, M. T., M. H. Costa, and E. A. Howard (2008), Simulating the surface waters of the Amazon River basin: Impact of new river geomorphic and flow parameterizations, *Hydrol. Processes*, *22*, 2542–2553, doi:10.1002/hyp.6850.

Decharme, B., H. Douville, C. Prigent, F. Papa, and F. Aires (2008), A new river scheme for global climate applications: Off-line evaluation over South America, *J. Geophys. Res.*, *113*, D11110, doi:10.1029/2007JD009376.

Döll, P., and B. Lehner (2002), Validation of a new global 30-min drainage direction map, *J. Hydrol.*, *258*, 214–231, doi:10.1016/S0022-1694(01)00565-0.

Döll, P., F. Kaspar, and B. Lehner (2003), A global hydrological model for deriving water availability indicators: Model tuning and validation, *J. Hydrol.*, *270*, 105–134, doi:10.1016/S0022-1694(02)00283-4.

Driscoll, N. W., and G. H. Haug (1998), A short circuit in thermohaline circulation: A cause for Northern Hemisphere glaciation?, *Science*, *282*, 436–438, doi:10.1126/science.282.5388.436.

Durand, M., K. M. Andreadis, D. E. Alsdorf, D. P. Lettenmaier, D. Moller, and M. Wilson (2008), Estimation of bathymetric depth and slope from data assimilation of swath altimetry into a hydrodynamic model, *Geophys. Res. Lett.*, *35*, L20401, doi:10.1029/2008GL034150.

Dutta, D., S. Herath, and K. Musiake (2000), Flood inundation simulation in a river basin using physically based distributed hydrologic model, *Hydrol. Processes*, *14*, 497–519, doi:10.1002/(SICI)1099-1085(20000228)14:3<497::AID-HYP951>3.0.CO;2-U.

Filizola, N., and J. L. Guyot (2004), The use of Doppler technology for suspended sediment discharge determination in the river Amazon, *Hydrol. Sci. J.*, *49*, 143–153, doi:10.1623/hysj.49.1.143.53990.

Hanasaki, N., S. Kanae, T. Oki, K. Masuda, K. Motoya, N. Shirakawa, Y. Shen, and K. Tanaka (2008), An integrated model for the assessment of global water resources—Part 1: Model description and input meteorological forcing, *Hydrol. Earth Syst. Sci.*, *12*, 1007–1025, doi:10.5194/hess-12-1007-2008.

Hess, L. L., J. M. Melack, E. M. L. M. Nobo, C. C. F. Bardosa, and M. Gastil (2003), Dual-season mapping of wetland inundation and vegetation for the central Amazon basin, *Remote Sens. Environ.*, *87*, 404–428, doi:10.1016/j.rse.2003.04.001.

Horritt, M. S., and P. D. Bates (2002), Evaluation of 1D and 2D numerical models for predicting river flood inundation, *J. Hydrol.*, *268*, 87–99, doi:10.1016/S0022-1694(02)00121-X.

Houweling, S., T. Kaminski, F. Dentener, J. Lelieveld, and M. Heimann (1999), Inverse modeling of methane sources and sink using the adjoint of a global transport model, *J. Geophys. Res.*, *104*(D21), 26,137–26,160, doi:10.1029/1999JD900428.

Kim, H., P. J.-F. Yeh, T. Oki, and S. Kanae (2009), Role of rivers in the seasonal variations of terrestrial water storage over global basins, *Geophys. Res. Lett.*, *36*, L17402, doi:10.1029/2009GL039006.

Krinner, G. (2003), Impact of lakes and wetlands on boreal climate, *J. Geophys. Res.*, *108*(D16), 4520, doi:10.1029/2002JD002597.

Lehner, B., and P. Döll (2004), Development and validation of a global database of lakes, reservoirs and wetlands, *J. Hydrol.*, *296*, 1–22, doi:10.1016/j.jhydrol.2004.03.028.

Lehner, B., K. Verdin, and A. Jarvis (2008), New global hydrography derived from spaceborne elevation data, *Eos Trans. AGU*, *89*(10), 93, doi:10.1029/2008EO100001.

Leopold, L., and T. Maddock (1953), The hydraulic geometry of stream channels and some physiographic implications, *U.S. Geol. Surv. Prof. Pap.*, 252.

Masutomi, Y., Y. Inui, K. Takahashi, and U. Matsuoka (2009), Development of highly accurate global polygonal drainage basin data, *Hydrol. Processes*, *23*, 572–584, doi:10.1002/hyp.7186.

Matthews, E., and I. Fung (1987), Methane emission from natural wetlands: Global distribution, area, and environmental characteristics of sources, *Global Biogeochem. Cycles*, *1*, 61–86, doi:10.1029/GB001i001p00061.

Matthews, E., I. Fung, and J. Lerner (1991), Methane emission from rice cultivation: Geographic and seasonal distribution of cultivated areas and emissions, *Global Biogeochem. Cycles*, *5*, 3–24, doi:10.1029/90GB02311.

Meade, R. H., J. M. Rayol, S. C. da Conceicaô, and J. R. G. Natividade (1991), Backwater effects in the Amazon River basin of Brazil, *Environ. Geol. Water Sci.*, *18*(2), 105–114, doi:10.1007/BF01704664.

Miller, J. R., G. L. Russell, and G. Caliri (1994), Continental-scale river flow in climate models, *J. Clim.*, *7*, 914–928, doi:10.1175/1520-0442(1994)007<0914:CSRFIC>2.0.CO;2.

Moussa, R., and C. Bocquillon (1996), Criteria for the choice of flood-routing methods in natural channels, *J. Hydrol.*, *186*, 1–30, doi:10.1016/S0022-1694(96)03045-4.

Oki, T., and S. Kanae (2006), Global hydrological cycles and world water resources, *Science*, *313*, 1068–1072, doi:10.1126/science.1128845.

Oki, T., and Y. C. Sud (1998), Design of total runoff integrating pathways (TRIP)—A global river channel network, *Earth Interact.*, *2*, 1–36, doi:10.1175/1087-3562(1998)002<0001:DOTRIP>2.3.CO;2.

Oki, T., T. Nishimura, and P. Dirmeyer (1999), Assessment of annual runoff from land surface models using total runoff integrating pathways (TRIP), *J. Meteorol. Soc. Jpn.*, *77*(1B), 235–255.

Papa, F., C. Prigent, F. Aires, C. Jimenez, W. B. Rossow, and E. Matthews (2010), Interannual variability of surface water extent at the global scale, 1993–2004, *J. Geophys. Res.*, *115*, D12111, doi:10.1029/2009JD012674.

Pavelsky, T. M., and L. C. Smith (2008a), Remote sensing of hydrologic recharge in the Peace-Athabasca Delta, Canada, *Geophys. Res. Lett.*, *35*, L08403, doi:10.1029/2008GL033268.

Pavelsky, T. M., and L. C. Smith (2008b), RivWidth: A software tool for the calculation of river width from remotely sensed imagery, *IEEE Geosci. Remote Sens. Lett.*, *5*(1), 70–73, doi:10.1109/LGRS.2007.908305.

Prigent, C., F. Papa, F. Aires, W. B. Rossow, and E. Matthews (2007), Global inundation dynamics inferred from multiple satellite observations, 1993–2000, *J. Geophys. Res.*, *112*, D12107, doi:10.1029/2006JD007847.

Rodriguez, E., C. S. Morris, and J. E. Belz (2006), A global assessment of the SRTM performance, *Photogramm. Eng. Remote Sens.*, *72*(3), 249–260.

Sanders, B. F. (2007), Evaluation of on-line DEMs for flood inundation modeling, *Adv. Water Resour.*, *30*(8), 1831–1843, doi:10.1016/j.advwatres.2007.02.005.

Sellars, C. D. (1981), A floodplain storage models used to determine evaporation losses in the upper Yobe River, northern Nigeria, *J. Hydrol.*, *52*, 257–268, doi:10.1016/0022-1694(81)90174-8.

Sophocleous, M. (2002), Interactions between groundwater and surface water: The state of the science, *Hydrogeol. J.*, *10*, 52–67, doi:10.1007/s10040-001-0170-8.

Sun, G., K. J. Ranson, V. I. Kharuk, and K. Kovacs (2003), Validation of surface height from shuttle radar topography mission using shuttle laser altimeter, *Remote Sens. Environ.*, *88*, 401–411, doi:10.1016/j.rse.2003.09.001.

Tapley, B. D., S. Battadpur, J. C. Ries, P. E. Thompson, and M. M. Watkins (2004), GRACE measurements of mass variability in the Earth system, *Science*, *305*, 503–505, doi:10.1126/science.1099192.

Trigg, M. A., M. D. Wilson, P. D. Bates, M. S. Horritt, D. E. Alsdorf, B. R. Forsberg, and M. C. Vega (2009), Amazon flood wave hydraulics, *J. Hydrol.*, *374*, 92–105, doi:10.1016/j.jhydrol.2009.06.004.

Wilson, M. D., P. D. Bates, D. Alsdorf, B. Forsberg, M. Horritt, J. Melack, F. Frappart, and J. Famiglietti (2007), Modeling large-scale inundation of Amazonian seasonally flooded wetlands, *Geophys. Res. Lett.*, *34*, L15404, doi:10.1029/2007GL030156.

Wolski, P., H. H. G. Savenije, M. Murray-Hudson, and T. Gumbricht (2006), Modelling of the flooding in the Okavango Delta, Botswana, using a hybrid reservoir-GIS model, *J. Hydrol.*, *331*, 58–72, doi:10.1016/j.jhydrol.2006.04.040.

Yamazaki, D., T. Oki, and S. Kanae (2009), Deriving a global river network map and its sub-grid topographic characteristics from a fine-resolution flow direction map, *Hydrol. Earth Syst. Sci.*, *13*, 2241–2251, doi:10.5194/hess-13-2241-2009.

Zanobetti, D., H. Longeré, A. Preissmann, and J. A. Cunge (1970), Mekong Delta mathematical model program construction, *J. Waterw. Harbors Coastal Eng. Div. Am. Soc. Civ. Eng.*, *96*, 181–199.

S. Kanae, Department of Mechanical and Environmental Informatics, Tokyo Institute of Technology, 2-12-1-W8-4 O-okayama, Meguro-ku, Tokyo 152-8552, Japan. (kanae@mei.titech.ac.jp)

H. Kim, Center for Hydrologic Modeling, University of California, 240E Rowland Hall, Irvine, CA 92612, USA. (hyungjun@uci.edu)

T. Oki and D. Yamazaki, Institute of Industrial Science, University of Tokyo, 4-6-1 Komaba, Meguro-ku, Tokyo 153-8505, Japan. (taikan@iis.u-tokyo.ac.jp; yamadai@rainbow.iis.u-tokyo.ac.jp)